2011

Comparison of modal analysis results of laser vibrometry and nearfield acoustical holography measurements of an aluminum plate

Jennifer L. Potter
Michigan Technological University

Follow this and additional works at: https://digitalcommons.mtu.edu/etds

Part of the Mechanical Engineering Commons

Recommended Citation

Potter, Jennifer L., "Comparison of modal analysis results of laser vibrometry and nearfield acoustical holography measurements of an aluminum plate", Master's Thesis, Michigan Technological University, 2011.
https://digitalcommons.mtu.edu/etds/399

Follow this and additional works at: https://digitalcommons.mtu.edu/etds

Part of the Mechanical Engineering Commons

COMPARISON OF MODAL ANALYSIS RESULTS OF LASER VIBROMETRY
AND NEARFIELD ACOUSTICAL HOLOGRAPHY MEASUREMENTS OF AN
ALUMINUM PLATE

By

Jennifer L. Potter

A THESIS

Submitted in partial fulfillment of the requirements for the degree of

MASTER OF SCIENCE

(Mechanical Engineering)

MICHIGAN TECHNOLOGICAL UNIVERSITY

2011

This thesis, "Comparison of Modal Analysis Results of Laser Vibrometry and Nearfield Acoustical Holography Measurements of an Aluminum Plate," is hereby approved in partial fulfillment of the requirements for the Degree of MASTER OF SCIENCE IN MECHANICAL ENGINEERING.

Department of Mechanical Engineering-Engineering Mechanics

Signatures:

Thesis Advisor   _____

Charles D. Van Karsen

Department Chair   _____

Dr. William W. Predebon

Date   _____

Table of Contents

List of Figures

List of Tables

Acknowledgements

First and foremost, I would like to thank my advisor, Chuck Van Karsen for providing the technical help, direction, patience and encouragement to finish this work. My gratitude also extends to committee members Dr. Jim DeClerck and Christopher Plummer.

Much appreciation goes to my team of mentors at The Boeing Company: Bernie Sklanka, Charlie Pickrel and John Mangus. Bernie was instrumental in determining the subject of this project, as well as being a constant source of NAH information and providing direction for this work and for life. Charlie is one of the brightest people I have ever had the pleasure to work with and his never ending excitement and eagerness to pass on his knowledge continues to impress and inspire me. And John, the hostile audience, kept me on my toes and ensured that I was always thinking about the next step. I would have not completed this without the help of these three.

Many thanks also go out to all the close friends who have seen the highs and lows of the last few years. Those that have volunteered to proof-read, who have been subjected to the online lectures streamed late at night, and who have been my moral support through this journey.

Lastly, I must thank my parents for their dedication to higher education and for being so supportive throughout my career.

Abstract

Noise and vibration has long been sought to be reduced in major industries: automotive, aerospace and marine to name a few. Products must be tested and pass certain levels of federally regulated standards before entering the market. Vibration measurements are commonly acquired using accelerometers; however limitations of this method create a need for alternative solutions.

Two methods for non-contact vibration measurements are compared: Laser Vibrometry, which directly measures the surface velocity of the aluminum plate, and Nearfield Acoustic Holography (NAH), which measures sound pressure in the nearfield, and using Green's Functions, reconstructs the surface velocity at the plate. The surface velocity from each method is then used in modal analysis to determine the comparability of frequency, damping and mode shapes. Frequency and mode shapes are also compared to an FEA model.

Laser Vibrometry is a proven, direct method for determining surface velocity and subsequently calculating modal analysis results. NAH is an effective method in locating noise sources, especially those that are not well separated spatially. Little work has been done in incorporating NAH into modal analysis.

Chapter 1: Introduction and Background

There are many industries interested in reducing noise and vibrations of their products: automobiles, airplanes, jigsaws, and even laptop computers. The noise or vibrations emitted from these products can be considered too loud or annoying, and in some cases can be dangerous to the users' health. Federal authorities limit the acceptable vibration or noise exposure limits – whether it is for a jigsaw operator or for a community surrounding an airport. Testing for noise and vibrations must be done prior to a product's release to ensure that it meets the set standards.

1.1   Vibration Measurements

The most common method for acquiring vibration measurements is to attach an array of accelerometers to the test article and tap it with a hammer, excite it with a mechanical shaker, or collect data during normal operating conditions. While this is an effective way of collecting the necessary data, there are applications in which this method would be inappropriate. When dealing with a small object or an object with little mass, it is impossible to add multiple accelerometers without changing the dynamics of the system – that is adding mass from the accelerometer(s) changes the resonant frequencies and damping factor of the test article. In industries where expensive prototypes are tested, it is undesirable to add glue or wax to a test article to adhere the accelerometers for testing. An alternative to the accelerometers is non contact measurements. Benefits to non-contact methods of vibration testing – other than eliminating the mass loading conundrum and the sticky mess of glue – include a potential decrease in setup and teardown time and

improved accessibility to a test article. Non contact measurement methods may also allow for testing under extreme conditions, such as very hot or cold temperatures, or in environments that do not allow for easy access, such as high-voltage areas or wind tunnels.

1.2   Non-contact Measurements

Laser vibrometry is a non-contact measurement technique that uses the principle of interferometry – the science of calculating the interference between two or more waves based on their superposition – to determine the velocity of the test subject (1). The measurement beam from the laser scanning head is directed at a point on the test article (this point must be mirror-like enough to reflect back to the laser head). The back-scattered light from this point interferes with the original beam at the laser head and is read with a photo detector. The vibrometer converts this signal into a voltage reading proportional to the surface velocity. The voltage is digitized before becoming the final output. See Figure 1.1 for a schematic of the working laser system. The laser is useful in extreme conditions (i.e. temperature), and can also be employed to measure test subjects that are far away, or too large or small for other methods. Generally a laser vibrometer can measure frequencies well into the hundred-thousand kHz range.
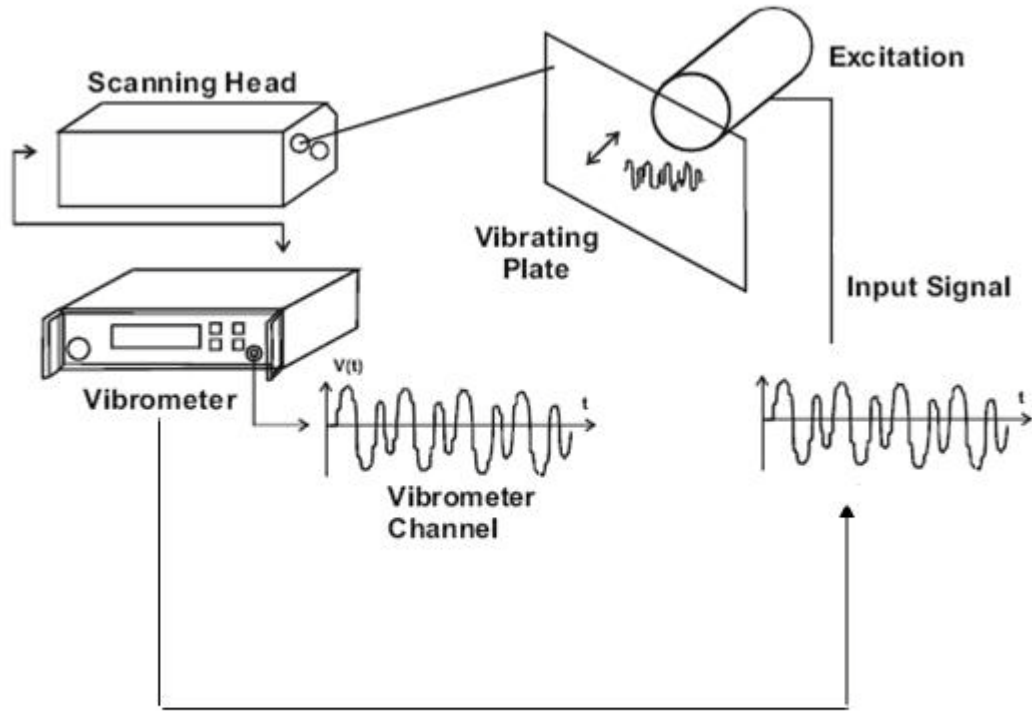
Figure 1.1: Schematic of Laser Vibrometer System (1)

Sound intensity is a non contact measurement technique that is typically used for noise

source identification, and is a measure of the sound power per unit area. Measurements

are taken by scanning an intensity probe over two directions (i.e. x and y) of a

predetermined surface area. The probe is made up two facing microphones separated by

a spacer; one measures "positive" energy– energy from the direction of the source, and

the other measure "negative" energy– energy from behind the probe. The data contain

pressure level, speed and direction of the sound waves. The final intensity value is a

function of the total surface area scanned, as well as the direction and amplitude of the

sound waves. The usable frequency range of sound intensity measurements is

3

determined by the spacing between the two microphones of the probe. Typical spacing is

12mm, which limits the upper range of the measurements to around 6 kHz. The lower

bound of the measurement is dependent on how well the two microphones are phase-

matched, but is generally 100Hz (3). Figure 1.2 illustrates intensity probes in use to

measure tire and pavement interaction noise.

Figure 1.2: Sound Intensity Measurements for Quieter Pavement Noise Research (2)

Beamforming acts as an acoustic camera to determine the location of multiple noise sources that may have very similar frequency content (3). A prime example of this is airplane noise flyover certification testing, as shown in Figure 1.3, where a large microphone phased array is placed on the runway to take a "picture" of the noise from the airplane as it flies over. The acoustic data is analyzed using a delay and sum strategy, where the noise from each section of the airplane (i.e. engines, landing gear, slats) is summed based on its phase delay to each of the microphones. This creates a large cross spectral density matrix. The data analysis produces a spectrogram of the data, which "maps" – or creates an acoustic picture of – the strength of each noise source. The array shown in Figure 1.3 consists of approximately 600 microphones, each being illustrated by a white spot on the black tarmac. Orange cables can also be seen running from the center of the array to the power and data ports on the edge of the tarmac.
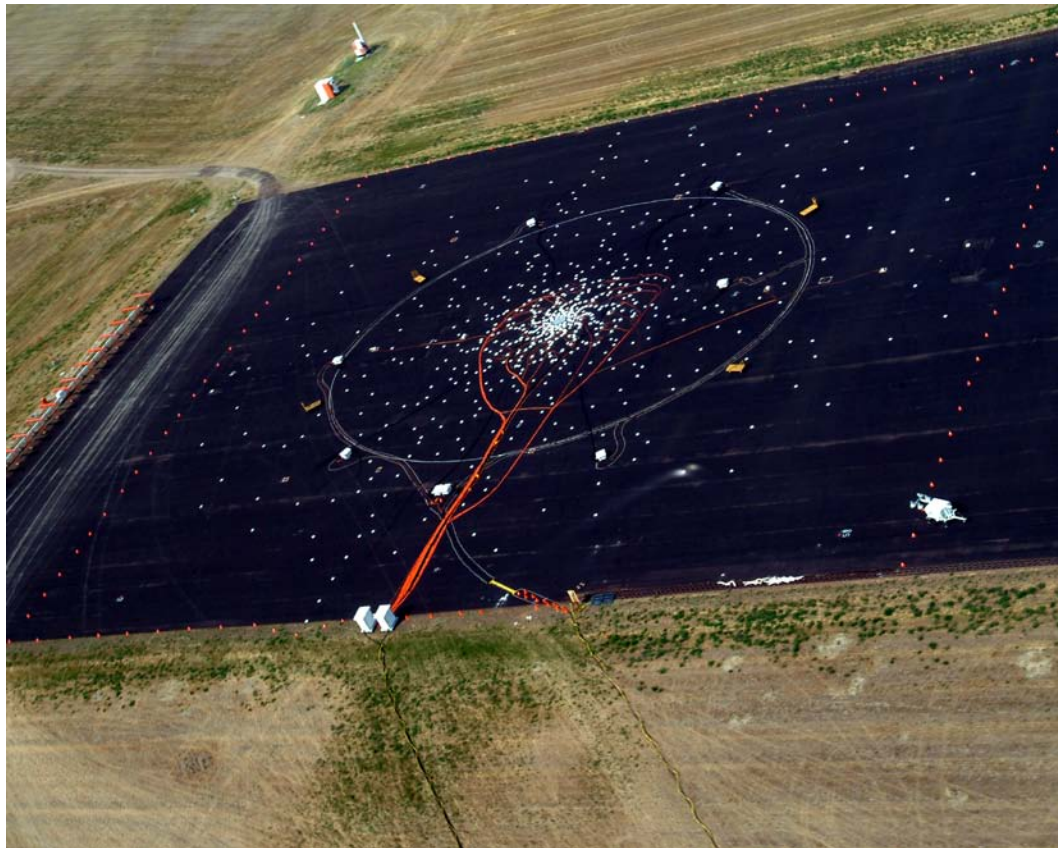
Figure 1.3: Phased Array used in Flyover Noise Testing

Nearfield acoustic holography (NAH) is a non contact method that is useful for measurements in both the acoustic and vibration fields (3). The basic principle of NAH is to measure a two-dimensional surface at a given distance from the source, then to mathematically reconstruct the three-dimensional field which can be projected to any surface at a finite distance from the source. These reconstructed quantities can be determined both nearer to and farther from the source, and has earned NAH the reputation of being called an "explosion of information" (4) due to its dense information content. The measured two-dimensional sound pressure levels can determine the three-dimensional sound pressure field, as well as the particle velocity field, acoustic intensity

field, and the surface velocity and intensity. These are determined through the boundary condition knowledge that the particle velocity at the surface is the same as the surface velocity. NAH is often used in noise source identification, due to the proximity of the measurement locations to the source (i.e. the nearfield), individual sources can be identified to a much finer resolution than measurements taken further from the source. NAH uses the evanescent waves in the reconstruction of the three-dimensional field, which are pertinent to determine the fine resolution. These waves decay to an immeasurable value within one wavelength from the source, which requires the measurements to be taken close to the source, or in the nearfield. Figure 1.4 illustrates an NAH array measuring the jet plume to study the characteristics of the noise field.

Figure 1.4: NAH Array Measuring Military Jet Aircraft Noise (5)

Table 1 provides a summary of comparison of the afore-mentioned vibration

measurement techniques:

Table 1.1
Comparison of Measurement Techniques

Method	Measures	Applications	Limitations
Accelerometers	Vibrations	Most types of vibration testing. Good for large or massive objects (i.e. airplanes, tires, solid structures).	Mass loading - not suitable for small objects (relative to size of accels). Must be semi-permanently attached to object (i.e. wax, glue, magnet, mechanical fastener).
Laser Vibrometry	Vibrations	Large or small, inaccessible objects, extreme conditions. Can be used to very high frequencies.	Laser head must be stationary, have clear line of sight and be within 20 degrees of normal.
Intensity	Acoustic	Noise source identification.	Commonly used for lower frequencies: below 6kHz.
Beamforming	Acoustic	Noise source identification.	Assume uncorrelated noise sources. Measurements must be made in the far field.
NAH	Both	Can be used to collect 3D information from a 2D measurement – will reconstruct sound pressure, particle velocity, intensity.	Computationally involved data reduction.

1.3 Laser vs. NAH study

Martarelli, Revel and Tomasini of the Universita degli Studi di Ancona in Italy compared laser vibrometer and NAH measurements in their 2002 paper, "Laser Doppler Vibrometry and Near-Field Acoustic Holography: different approaches for surface velocity distribution measurements" (6) . The goal of the study was to determine if the two methods were able to both determine surface velocity with measurement uncertainty below 2-3%, for a frequency range up to 5000 Hz. It also sought to determine the capability of measuring mode shapes in various applications, measuring objects with complex shapes and determining the velocity component of the object. Both methods were used to measure surface velocity of a free-free steel plate, which was excited by a shaker providing white noise from 20 Hz to 20 kHz. The laser scanned 532 points – a grid of 19 by 28 – giving a spatial resolution of 0.021m. The measured frequency range was set to 0 to 5 kHz, and the frequency resolution was 1.5625 Hz. NAH measurements were analyzed between 0 and 3 kHz. The frequency resolution for these measurements ranged from 10 to 20 Hz; the spatial resolution was kept consistent with that of the laser measurements. The results of this study compared the directly measured surface velocity from the laser vibrometer and the calculated surface velocity from the NAH measurements. It was determined that the difference in resonant frequency content between the two methods was within 1%, implying that the two methods are satisfactorily comparable. It was also determined through a visual inspection that the mode shapes also correlate qualitatively. Furthermore, a Modal Assurance Criterion (MAC) Matrix – a tool used to determine whether or not modes shape vectors are the parallel – showed higher values, indicating a quantitative agreement of 83% or better.

9

1.4   Proposed Work

While the Italian study of the laser comparability with NAH provided a platform from which to base this work on, it does not delve as deep into the comparison of results as this project will.   Martarelli, et al looked at the frequency content and a quantitative comparison of mode shape vectors. This project will also investigate the damping and use more tools to quantitatively compare the mode shapes. Furthermore, the experimental data will be compared to analytical frequency and mode shapes. These comparisons will be useful in determining the feasibility of using NAH and Laser Vibrometry in field testing situations.

Vibration data for comparison will be acquired on a free-free aluminum plate using NAH and Laser Vibrometry methods. The Laser will directly measure the surface velocity and produce Frequency Response Functions (FRF) for use in comparison. The holography array will measure sound pressure levels in the nearfield which will be used to construct the surface velocity of the plate, which will subsequently be used to calculate a psuedo FRF – in this case the surface velocity normalized to the input autopower. Chapter 2 will be devoted to the theory and limitations of these techniques, as well as experimental limitations.

The experimental setup will be addressed in Chapter 3. Processes for data acquisition and data reduction will also be covered.

Chapter 4 will present the results from both the NAH and Laser Vibrometry

measurements. It will also cover the analytical results.

In Chapter 5, conclusions from both testing methods and the analytical results will be

explored. It will include recommendations for future work in this area.

Chapter 2: Theory

The two measurement techniques will be discussed in this chapter. Background and theory will be given for each. The theory of modal analysis will also be discussed.

2.1   Holography

The basis of holography is to measure a wave field on a two dimensional surface and use that measurement to calculate the corresponding three dimensional fields. This can be done within acoustic, electromagnetic, or optical fields. An example of an optical hologram is shown in Figure 2.1.
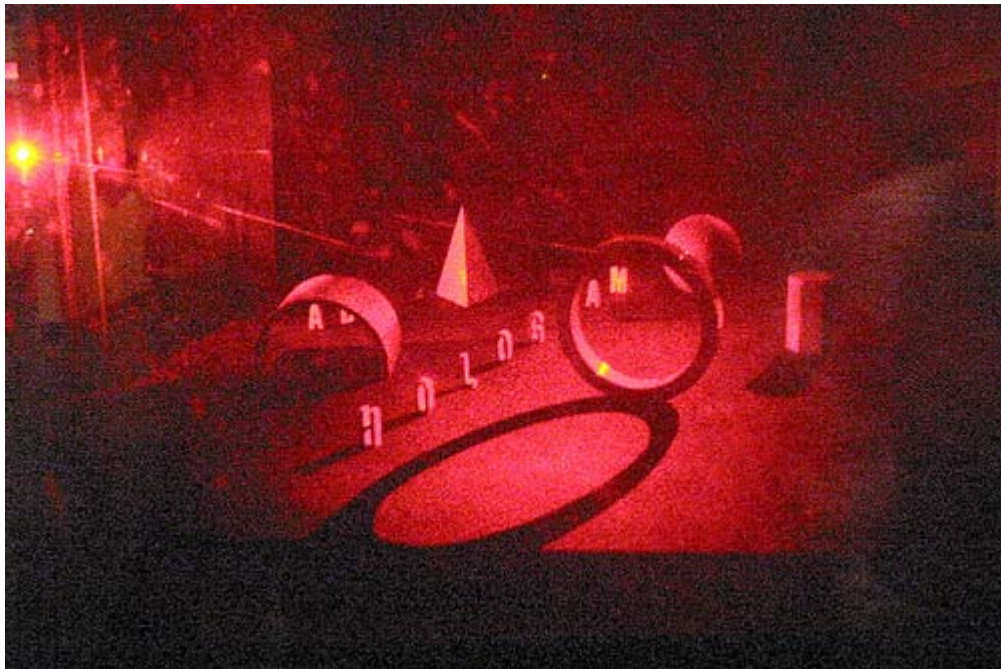

Figure 2.1: Hologram Art at the MIT Museum (7)

2.2   Acoustic Holography

Acoustic holography is a subset of holography where sound pressure measurements are taken on the two dimensional surface. This set of measurements uses the knowledge that these fields obey the acoustic wave equation, and that the construction of the three dimensional field can be determined through the use of Green's functions (8). The specific Green's function to be used is based on the boundary condition of the measurement, and explains the behavior of the wave field between the measurement surface location and the constructed hologram surface. To construct the three dimensional field, the calculation is a convolution of the two dimensional measurement with the appropriate Green's function in wave number space. A schematic of a typical acoustic holography set up is shown in Figure 2.2. The microphone array is placed a known distance from the test article and the sound pressure field is back-propagated using Green's functions from the array to the test article.
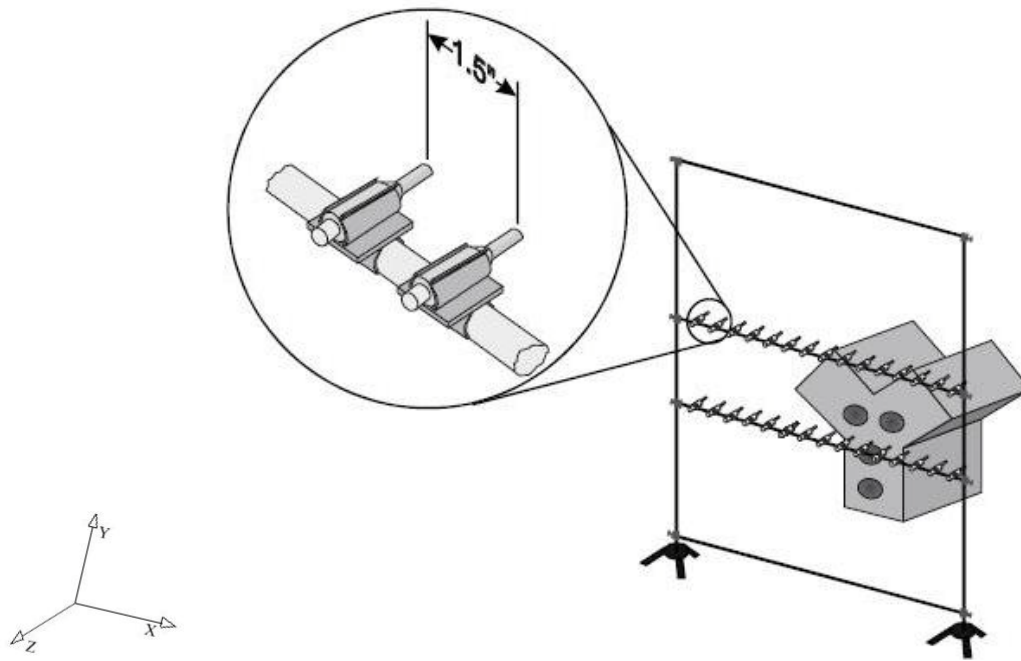
Figure 2.2: Acoustic Holography array Setup to Measure an Engine Block (9).

2.3   Nearfield Acoustical Holography

Nearfield Acoustical Holography (NAH) is a special case of acoustic holography in

which measurements are taken "close" to the radiating source. "Close" is defined as less

than half of a wavelength of the lowest emitted frequency of the source. The waves

measured in this region are known as evanescent waves, and decay to an immeasurable

value within one wavelength (4). The NAH calculations include both the normal

propagating waves and the evanescent waves in the reconstruction of the hologram

surface. This allows finer resolution of the radiating sources and determination of

individual noise sources separated by less than half of a wavelength; neglecting to

measure these will limit the spatial resolution of the reconstruction. The evanescent

waves appear in the wave equation as the imaginary term and are necessary to fully

characterize the sources; excluding these would only produce the behavior of the source

in the farfield. The difference between an evanescent wave and an ordinary propagating

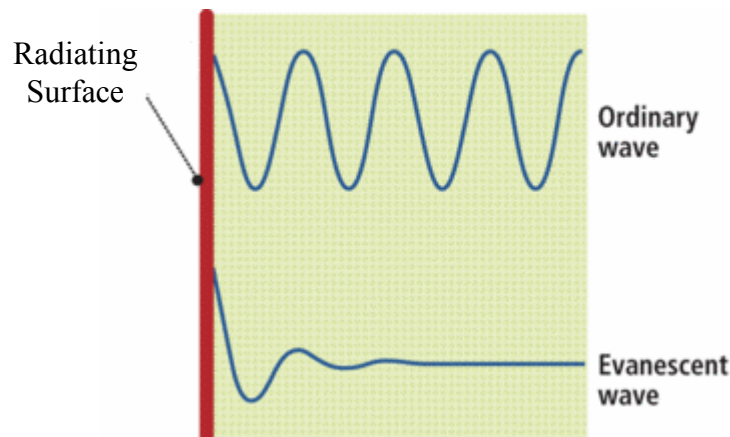wave can be seen below in Figure 2.3.

Figure 2.3: Ordinary Propagating Wave and Evanescent Wave

An array in the nearfield is shown in Figure 2.4. It can be seen here that the array is

approximately one inch from the test article, allowing evanescent waves to be captured.

The process to construct the projected hologram surfaces begins with sound pressure

measurements on a two dimensional surface. The microphone array must be evenly

spaced in the x and y directions, and the measurements must have a constant sampling

frequency. If the array is not large enough to measure the entire test article in one scan,

then a consistent reference channel must be used to tie all scans back together. This and

other practical limitations will be discussed later in this chapter. It can also be seen in

Figure 2.4 that the array is measuring evenly spaced x and y locations, indicated by the reflective dots on the panel.
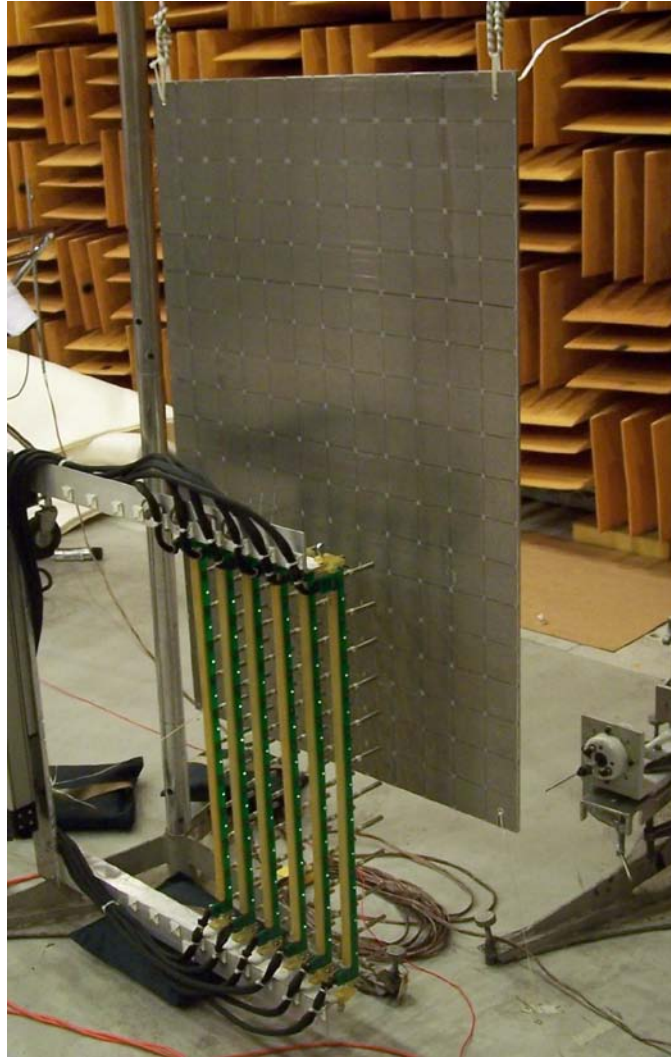

Figure 2.4: NAH Array set up to Measure a Flat Panel

The temporal Fourier transform of the data is taken to convert it to the frequency domain, and then a two dimensional spatial Fourier transform is performed along both the x and y directions of the measurement array to transform it to the wave number domain. The

wave number is crucial in the Green's function that will be used: $e^{ik_z z}$, where

$k_z = \sqrt{k^2 - (k_x^2 + k_y^2)}$. If k_z is real, the pressure waves propagate from the source varying

in phase. If k_z is imaginary, the waves vary in magnitude and decay exponentially with

distance from the source. The latter waves are the evanescent waves (4).

The wave number domain is based on the wave number, $k = \dfrac{2\pi f}{c}$, where c is the speed

of sound and f is the frequency of interest. The wave number, k, can be broken down into

spatial components such that $k = \sqrt{k_x^2 + k_y^2 + k_z^2}$ for each frequency. The x and y

directions indicate the two dimensional surface that the measurements are being taken,

while the z direction indicates the direction of travel of the propagating waves between

the measurement surface and the constructed hologram surfaces. Since k is a constant at

each frequency, the spatial components are not independent. Furthermore, since c, the

speed of sound, is different between an aluminum plate and air, the wavenumber, and

therefore the wavelength, of the frequency in each medium will be different. This

difference causes the plane wave to slightly change direction as it radiates from the plate

and couples with the air, at an angle, α. There becomes a frequency at which α

approaches zero and the plane waves no longer propagate from the plate, but travel

parallel to it (10).

The radiation circle is defined with radius, $k = \sqrt{k_x^2 + k_y^2 + k_z^2}$ in the wavenumber

domain; it is shown in Figure 2.5 in the x and y dimensions. The points on the circle

17

represent various propagating waves. Point A is a plane wave that is propagating at angle

α. Point B is a plane wave propagating normal to the plate surface, in which the pressure

varies with phase. Point C is a plane wave that is at the critical frequency, where the

waves become evanescent, travel parallel to the surface and begin to decay exponentially.

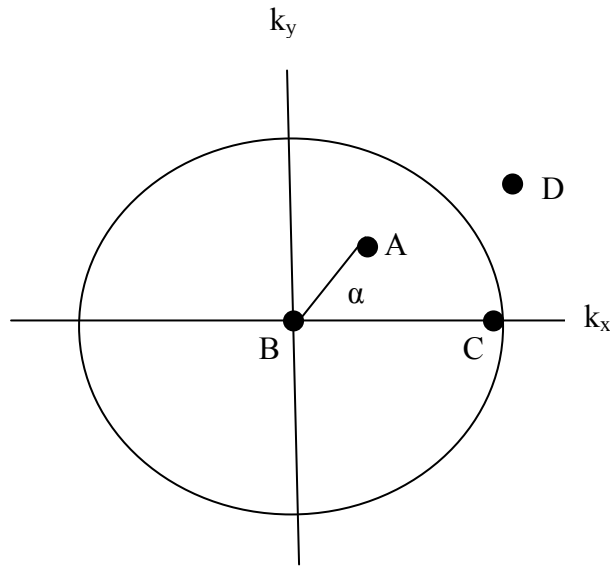Point D is a completely evanescent wave, with both x and y directional components.

Figure 2.5: Radiation Circle in Wavenumber Domain

2.4   Computational NAH

As previously mentioned, holography calculations assume that the field obeys the

acoustic wave equation:

$$\nabla^2 \varphi - \frac{1}{c^2} \frac{\partial^2 \varphi}{\partial t^2} = 0 \qquad (2.1)$$

Where c is the speed of sound and φ is the acoustic pressure, measured for all time

$(-\infty < t < +\infty)$, subjected to the Laplace Operator (∇^2). The FFT of the data is taken

with the applied window to transform the data into the frequency domain. Since infinite

time cannot be measured and pure sine wave testing will not be used in this case, a

window (i.e Hanning) should be applied to the time data to reduce the leakage error.

Then the 2D spatial FFT with filter is taken along both the x and y axis to analyze each

individual frequency in the wave number domain. The spatial, or wave number filter,

works in much the same way that a temporal filter does: the array edges are forced to

zero to minimize spatial leakage. By analyzing a single frequency, a single wave number

and wave length are also being analyzed (4). The field in the wave number domain must

satisfy the Helmholtz equation:

$$\nabla^2 \varphi(r) + k^2 \varphi(r) = 0 \tag{2.2}$$

From here, a known Green's function is used to construct the hologram surface. It is

assumed that the hologram surface is at a finite, known distance from the measurement

surface. It is also assume that the equation satisfies the Dirchlet boundary surface

condition: $e^{ik_z z}$. With this known boundary condition, the hologram surface is calculated

through surface integration – convolving the Green's function with the wave field at the

measurement surface. This is shown in the following equation, which is Rayleigh's

second integral, evaluated over all x and y:

$$\varphi(x, y, z) = -\frac{1}{2\pi} \iint \varphi(x', y', z') \frac{\partial}{\partial z'} [\frac{e^{ik(z-z')}}{z - z'}] dx' dy' \tag{2.3}$$

Then, the inverse spatial FFT is done to transform the data from wave number space back

to the frequency domain, producing φ at the hologram surface. If desired, the sound

pressure can be converted to intensity or particle velocity at this point. For the case of this study, the sound pressure was converted to particle velocity with the following equation:

$$u = \frac{-1}{j\omega\rho_o}\frac{\partial p}{\partial x} \tag{2.4}$$

Where u is the particle velocity, ρ_o is the air density, and p is the sound pressure (11).

A graphical representation of the computational process is below in Figure 2.6. Here the process is shown starting from raw time data, to which a window and FFT are applied. A single frequency is analyzed via the spatial FFT in the wave-number domain. The Green's function and boundary condition are applied and the data constructed the hologram surface. A spatial inverse FFT is performed to bring the sound pressure data back to the frequency domain. Here the sound pressure can be converted to velocity or surface intensity. In this study, the velocity frequency domain data (FRF's) will be used to do modal analysis. If necessary, an inverse FFT can be taken to create the new time history data at the hologram surface.
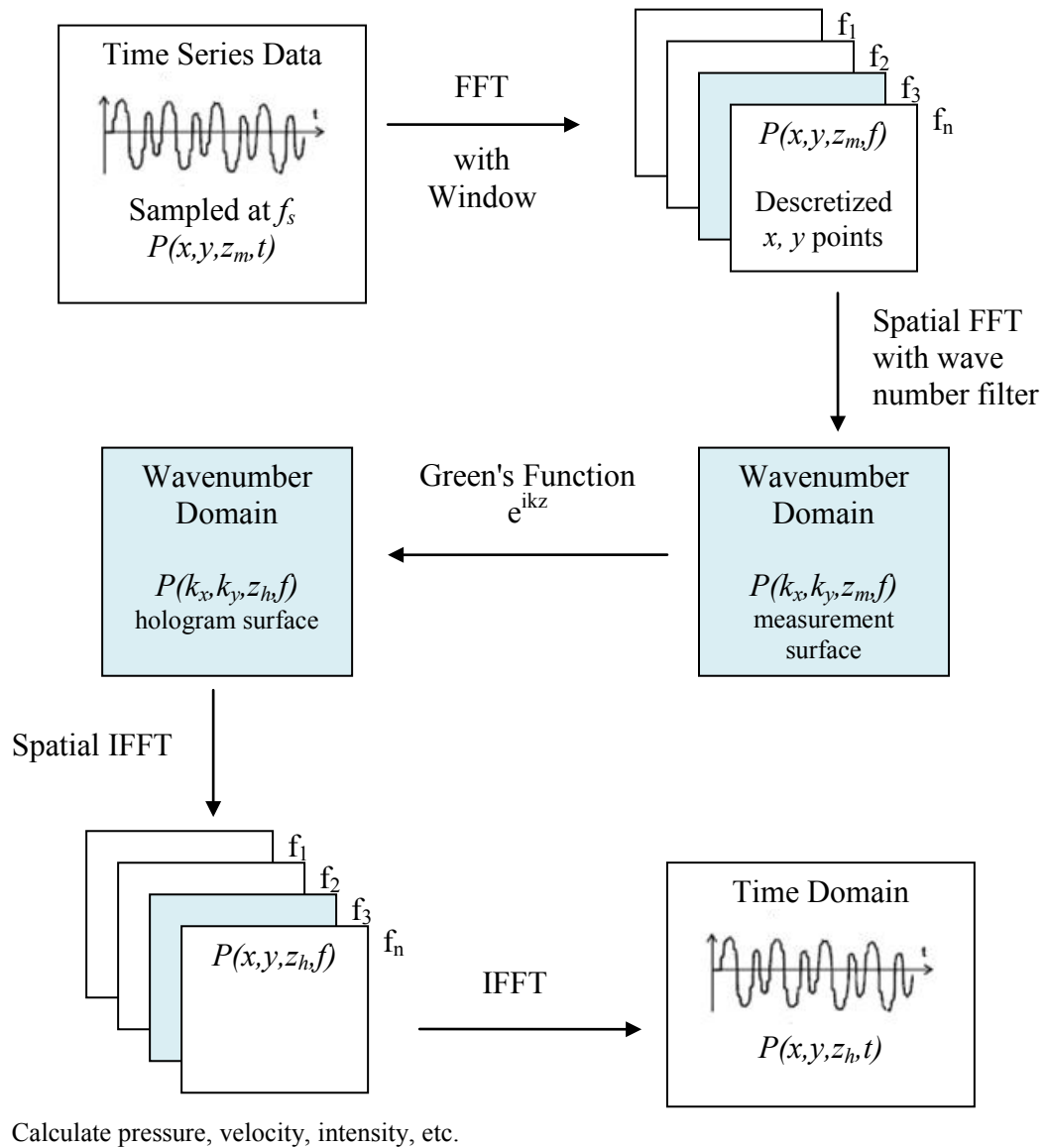
Figure 2.6: Computation Holography Process

2.5   Practical NAH

When taking NAH measurements of a test article in steady state, it may not be possible to

acquire all the array points at once. Making the assumption that the test article will

behave consistently through out the data acquisition, the microphone array can be broken into sub-arrays, but each sub-array measurement must have one consistent or repeated measurement channel for use in correlating the sub-arrays. The microphone spacing determines the maximum structural frequency available; to increase the maximum frequency, the microphone spacing must be decreased. The microphone spacing also determines the spatial resolution of the reconstructed pressure field. To avoid aliasing errors, a well used guideline is that the maximum microphone spacing must be less than one-half wavelength of the maximum frequency of interest (8). The lowest frequency is determined by the dimension of the total array, which should be at least one wavelength of the lowest frequency of interest.

Spatial noise is a concern when working with a large array of microphone and therefore a spatial filter should be applied. These spatial errors in the pressure measurements can be a product of microphone positioning or calibration errors, phase-mismatched microphones, random noise in the microphone measurements, and non-stationary errors in scanned data (moving the sub-array). When the hologram surface is constructed, the higher wave numbers are amplified more because the amplitude is a function of the number of wavelengths, and therefore produces more spatial noise at these wave numbers. To reduce this, in the wave number domain, a low-pass filter is applied to remove the spatial noise. The pressure at the full array boundary must be zero to avoid spatial leakage. This is comparable to applying a window to the time series data to ensure that the beginning and end of the dataset is zero. As the ends of the time series

period must be zero to avoid leakage, the spatial ends in the x and y directions must also be zero to avoid spatial leakage.

2.6 Laser Vibrometry

The laser vibrometer was used to directly measure the surface velocity of the panel for comparison to NAH. The environment was ideal for use of the laser because the laser head and panel were both stationary and the laser had a clear line of sight to the panel. Motion of the laser head is imparted to the signal, as is in-plane motion of the test article. The reflective dots were added to ensure that the scanning head could easily locate the measurement point and that the point would have sufficient backscattered light for the laser to acquire. This "retro-reflective material" is recommended to be used for measurements farther than one meter from the scanning head. The scanning head was set up to avoid standoff distances (between the laser head and test article) that may have minimized backscattered light. It was also set up so that the beam would be perpendicular to the center of the panel, keeping it within the required +/- 20 degrees of the laser at the sides, top and bottom of the panel. It should also be noted that there will be a small amount of cosine error at any point for which the laser beam is not normal to the surface, but is not an issue of concern until it reaches the 20 degree threshold. The laser software does not auto-range at each point, and must be set to measure the highest amplitude on the test article. Because of this, measurement quality can be poor at points where there is minimum motion (1). A set up of the Laser Vibrometer and a test article can be seen in Figure 2.7.

Figure 2.7: Laser Vibrometer and Test Article.

2.7   Modal Analysis

The theory behind modal analysis has been well documented. It is fully explained by

Randy Allemang, *Vibrations: Analytical and Experimental Modal Analysis* (12) and

Heylen, et al, *Modal Analysis Theory and Testing* (13). A brief summary is given below:

The modal analysis process uses the Frequency Response Function (or pseudo-FRF in the

case of NAH) to determine the natural frequency, damping and mode shapes of the

system. The process begins with the FRF in the frequency domain. For a simple single

degree of freedom (DOF) system the FRF is expressed as:

$$H(j\omega) = \frac{X(j\omega)}{F(j\omega)} \qquad (2.5)$$

In which X is the response and F is the input force, both as a function of frequency. The

FRF can be rewritten in terms of the roots of the characteristic equation, with m

representing the mass of the system:

$$H(j\omega) = \frac{1/m}{(j\omega - \lambda_1)(j\omega - \lambda_2)} \qquad (2.6)$$

Where $\lambda_1 = -\sigma + j\omega_d$ and $\lambda_2 = -\sigma - j\omega_d$, which are the poles of the system (note

$\lambda_1 = \lambda_2*$). The real part, σ, represents the damping factor and the imaginary part, $j\omega_d$,

represents the damped natural frequency. (Using partial fraction expansion, the FRF can

be written in terms of poles and residues (A):

$$H(j\omega) = \frac{A}{(j\omega - \lambda*)} + \frac{A*}{(j\omega - \lambda*)} \qquad (2.7)$$

These equations are the simplest form for a single degree of freedom system. A multiple

DOF system has N resonancies described by the poles, λ_r, and associated mode shape

vectors, $\{\Psi_r\}$. The partial fraction form of the FRF is given as:

$$H_{pq}(j\omega) = \sum_{r=1}^{N} \frac{A_{pqr}}{(j\omega - \lambda_r*)} + \frac{A_{pqr}*}{(j\omega - \lambda_r*)} \qquad (2.8)$$

Where the residues are scaled products of the mode shape vector components:

$$A_{pqr} = Q_r \psi_{pr} \psi_{qr} \qquad (2.9)$$

Experimental modal analysis uses a parameter estimation algorithm using the FRF to find the poles and residues of the system. Two curve fitting algorithms were used in modal analysis: the Eigenvalue Realization Algorithm (ERA) is a first order time domain algorithm, and Polyreference Time Domain (PTD) is a higher order time domain algorithm (16). Both methods assume an impulse input at time, $t = 0$, and all forcing functions to be 0 at time $t > 1$. Both also use time iterations to create an overdetermined problem, and assume that the number of measured outputs greatly exceeds the number of measured inputs ($N_o >> N_i$). In each case, the general multiple input, multiple output (MIMO) equation can be written as:

$$\sum_{k=0}^{m}[\alpha_k][h(t_{i+k})] = 0 \qquad (2.10)$$

Where α is the numerator polynomial matrix coefficient and h is the Hankel matrix. ERA assumes low order ($m=1$) and uses matrices of size $2N_o$ by $2N_o$:

$$[[\alpha_0]]_{2NoX2No}\begin{bmatrix}[h(t_{i+0})]\\ [h(t_{i+1})]\end{bmatrix}_{2NoX2Ni} = -\begin{bmatrix}[h(t_{i+1})]\\ [h(t_{i+2})]\end{bmatrix}_{2NoX2Ni} \qquad (2.11)$$

PTD assumes a high order ($m>2N/N_i$, that is twice the number of modes to be found by the number of inputs), and uses matrices of size N_i by N_i:

$$[[\alpha_0] \quad [\alpha_1] \quad ... \quad [\alpha_{m-1}]]_{NiXmNi}\begin{bmatrix}[h(t_{i+0})]\\ [h(t_{i+1})]\\ ...\\ [h(t_{i+m-1})]\end{bmatrix}_{mNiXNoi} = -[[h(t_{i+m})]]_{NiXNo} \qquad (2.12)$$

It is expected that these parameter estimation methods will produce slightly different results and both will be used to estimate the modes.

Chapter 3: Experiment

This chapter covers the experimental set up, data acquisition and experimental limitations. Data processing parameters will also be discussed.

3.1 Experimental Setup

Data for this experiment were acquired in the Experimental Test Facility (ETF) in the Aero/Noise/Propulsion/Structural Dynamics (ANPSD) Laboratory at The Boeing Company in Seattle, WA. The room is a hemi-anechoic chamber with a separate control room. The walls and ceiling are covered in foam wedges, and the floor is concrete. The room measures 42 feet wide by 29 feet long by 17 feet high.

An aluminum (Al-2024) plate of dimensions 24" x 36" x 0.25" was hung vertically with 1/8" diameter bungee cords from a horizontal rod, with the top of the panel approximately four feet from the floor, which put the bottom edge of the panel one foot from the floor. This set up can be seen in Figure 3.1.
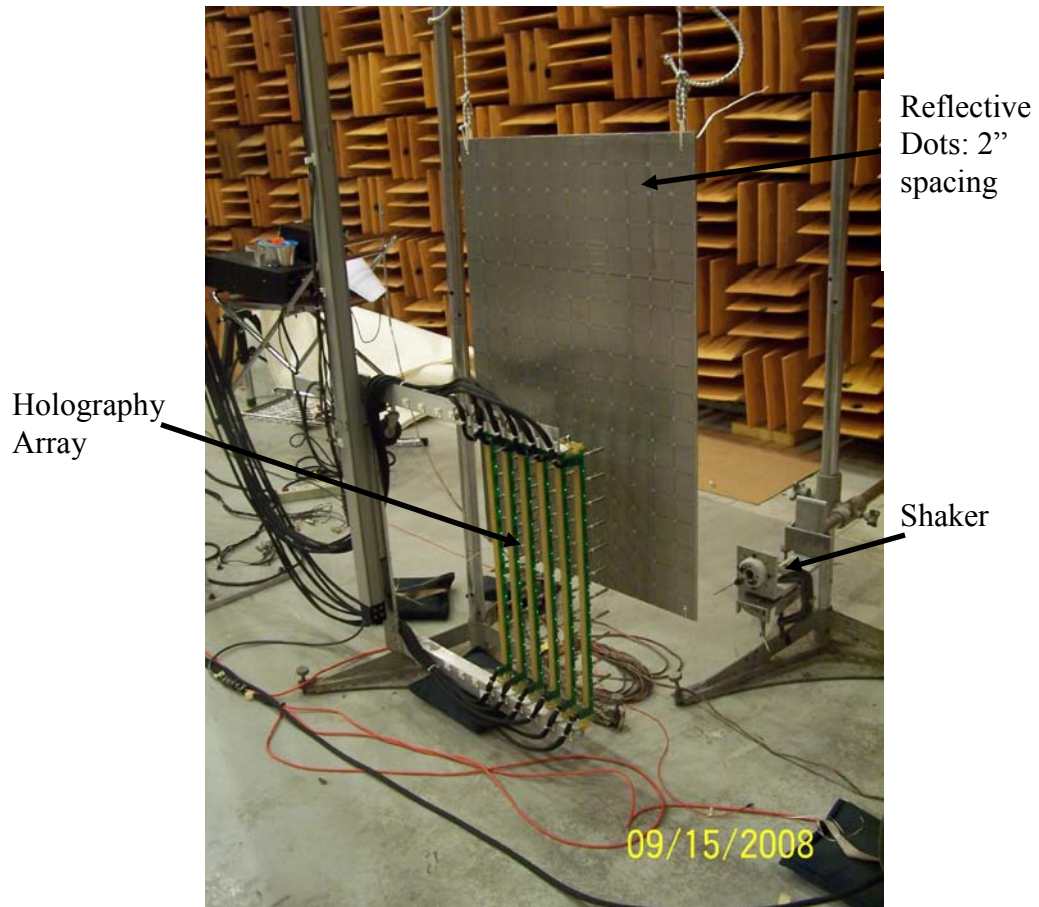
Figure 3.1: View of front of panel – reflective dots & NAH array

A two inch grid was drawn on the plate to locate the reflective tape for the laser measurements. The NAH microphone measurement locations were also taken on this grid. Five 20" strips of three inch wide 3M damping tape #435 were applied to the opposite side to add a small amount of damping to the plate. The amount of damping tape added intended to damp the plate enough to cause the vibrations to decay within a given time segment, which was 2.5 seconds in this case, and was necessary to prevent leakage. See figure 3.2.
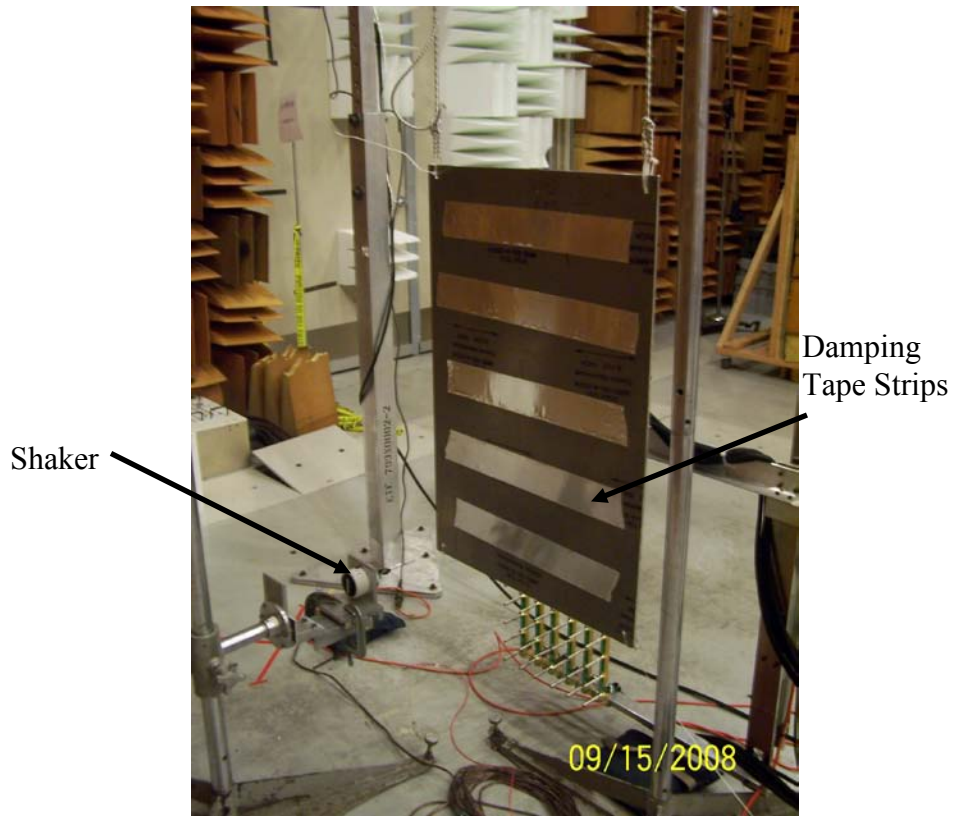
Figure 3.2: View of back of panel – damping tape & shaker setup

Reflective dots were attached to the plate at the intersections of the grid (see figure 3.1 - front view of panel), for use in the laser vibrometer measurements. A Ling Dynamic Systems (LDS) V102 shaker was attached to the bottom right corner of the plate to provide the excitation – both with random and burst random noise – and amplified using an LDS Star 1.0 amplifier. The shaker was driven by the Polytech Scanning Vibrometer Software 8.51 for both the laser and NAH measurements. The laser vibrometer was situated normal to the hanging plate at a distance of approximately 8 feet and acquired 30 averages at each of the 247 measurement locations – taking approximately four and a half hours to completely acquire one set of random data. The panel and shaker setup was

enclosed by a wall of foam wedges to reduce any noise data contamination. For the first

set of data, random noise was used to excite the panel. The laser vibrometer acquired

FRF's at a sampling rate of 16 kHz, giving a 0.5 Hz resolution in the data. A Hanning

window was applied to both the laser and force input measurements; 50% overlap and

12,800 FFT lines were used. The test was repeated and parameters kept constant for the

burst measurements, except that a rectangular window was applied to both the laser and

force channels and a burst length of 50% on, 50% off was used. The reference transducer

for all measurements was the load cell on the shaker. See figure 3.3 for a schematic of

the laser setup.
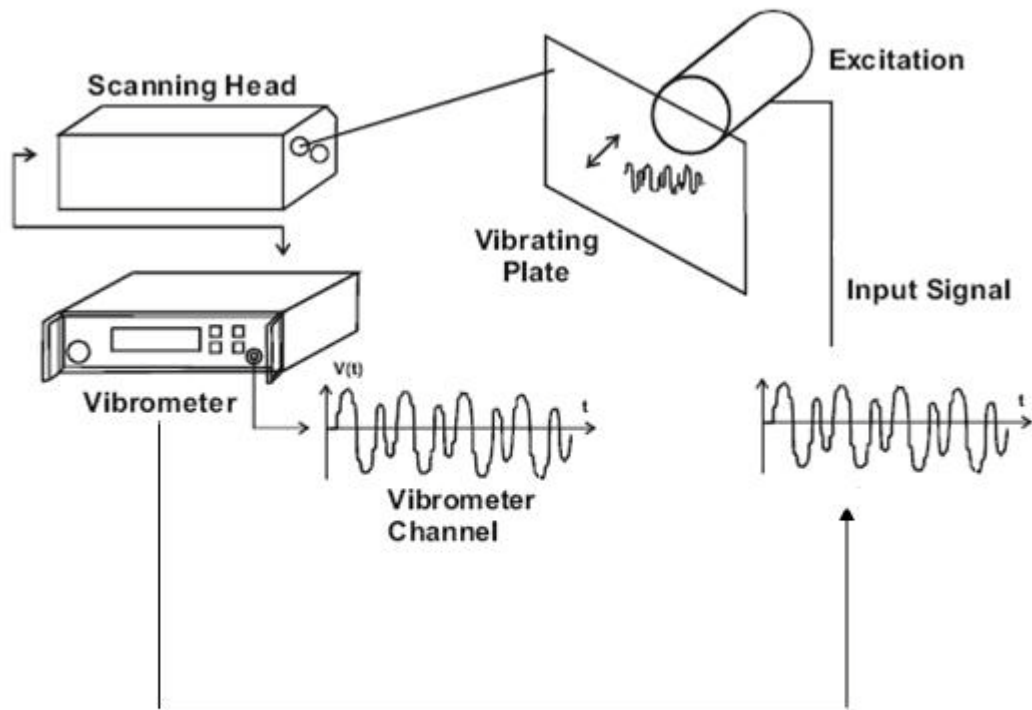
Figure 3.3: Schematic of Laser Vibrometer Setup (1)

The Laser Vibrometer was only capable of recording FRF data or time data in one run. Since FRF was the desired end result, the test was not run a second time to capture the raw time data.

When the laser measurements were complete, a computer controlled microphone array positioning device was set up in front of the panel. The arm of this device was positioned using Parker CompuMotion software, which drove a Parker CompuMotor 6200 series controller which allowed microphone positioning to 1/36" accuracy (see figure 3.4).
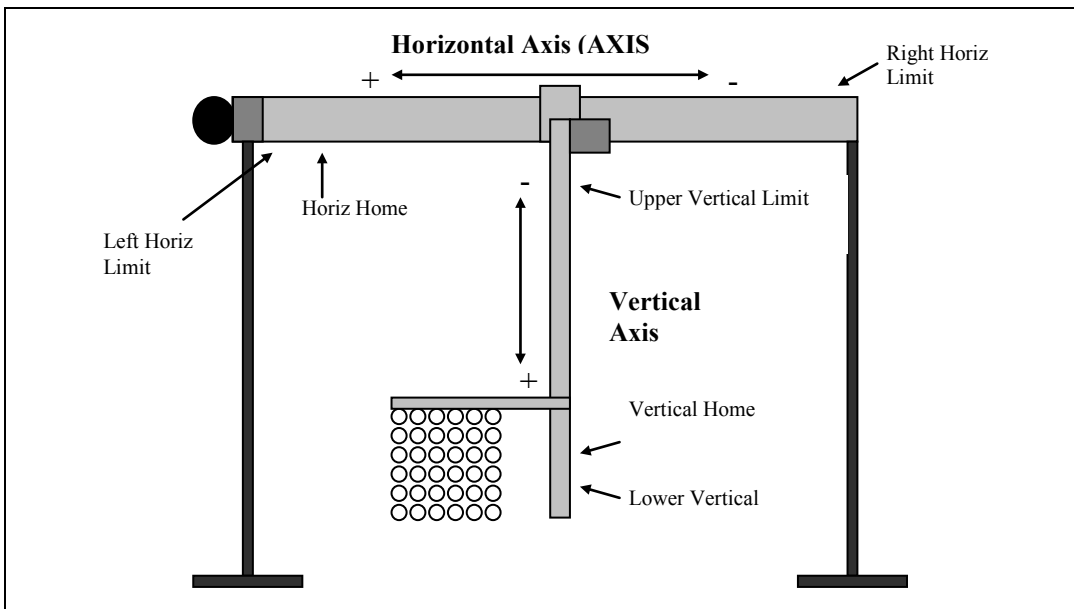
Figure 3.4: NAH Array positioning device

The array held a 12 x 6 grid of quarter-inch GRAS Type PR40A microphones spaced at two inches in both the x and y directions. The grid was set up in the x-y plane, parallel to

the plate. The bottom, left corner of the plate was made the origin (0,0,0), so that the array was at z = 1 inch. The shaker was then set to (24, 0, 0) in the bottom right corner of the plate, which was consistent from the Laser measurements. See figure 3.5.
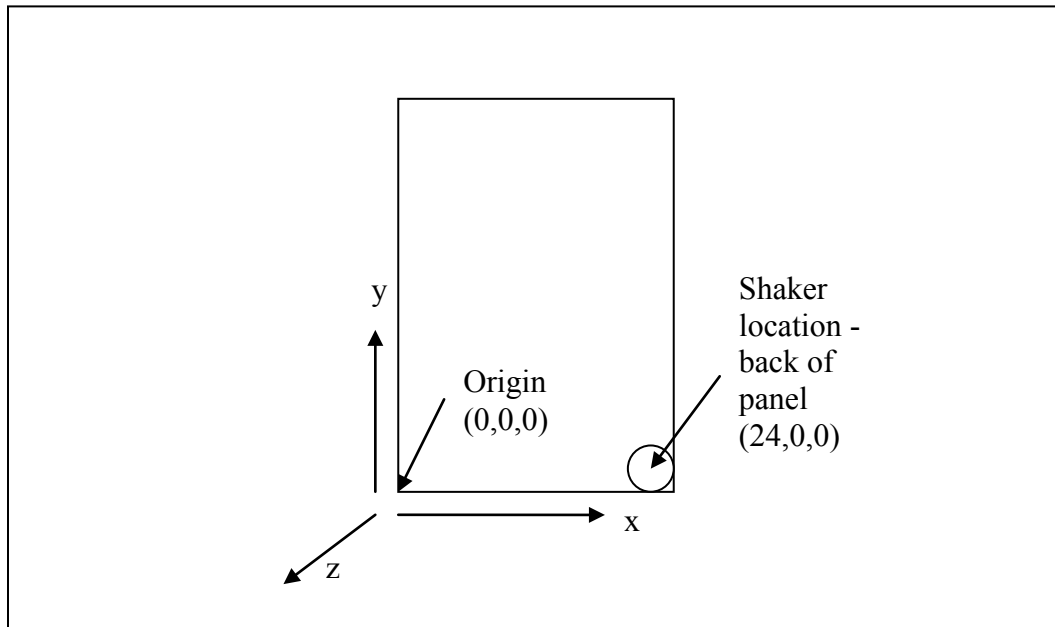
Figure 3.5: Geometry of plate and array – facing the panel.

The microphone array measurement locations lined up with the Laser measurement locations. The sub-array acquired sound pressure time history data in six different locations on the plate for a total array size of 24 x 18 points, or 46 x 34 inches. This extended array size allowed the pressure measurements to reach zero on the outer limits of the plate and avoided spatial leakage and wraparound error in the data processing. A schematic of the six array positions is shown in Figure 3.6:
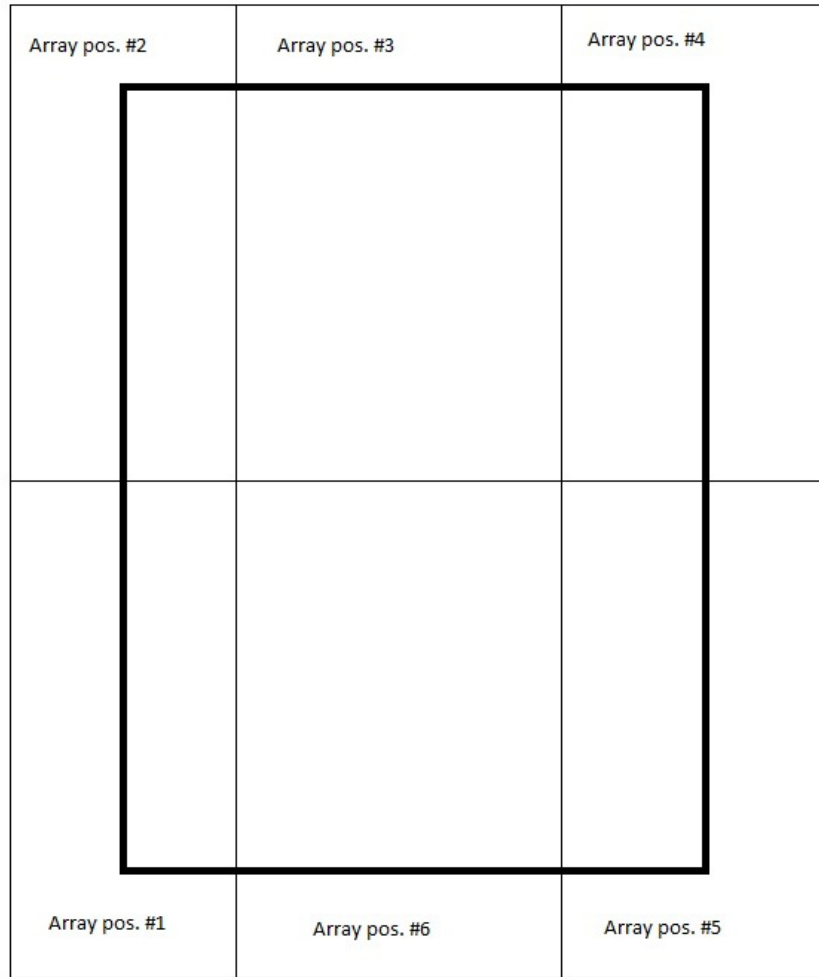
Figure 3.6: Microphone Array Scanning Positions

The microphone array was connected to a Boeing-built signal processing unit

(Holography Array Microphone Power Supply: HAMPS), which applied a 20dB gain to

all signals, then to a Sony SIR1000 tape recorder. See Figure 3.7 for a schematic of the

set up.
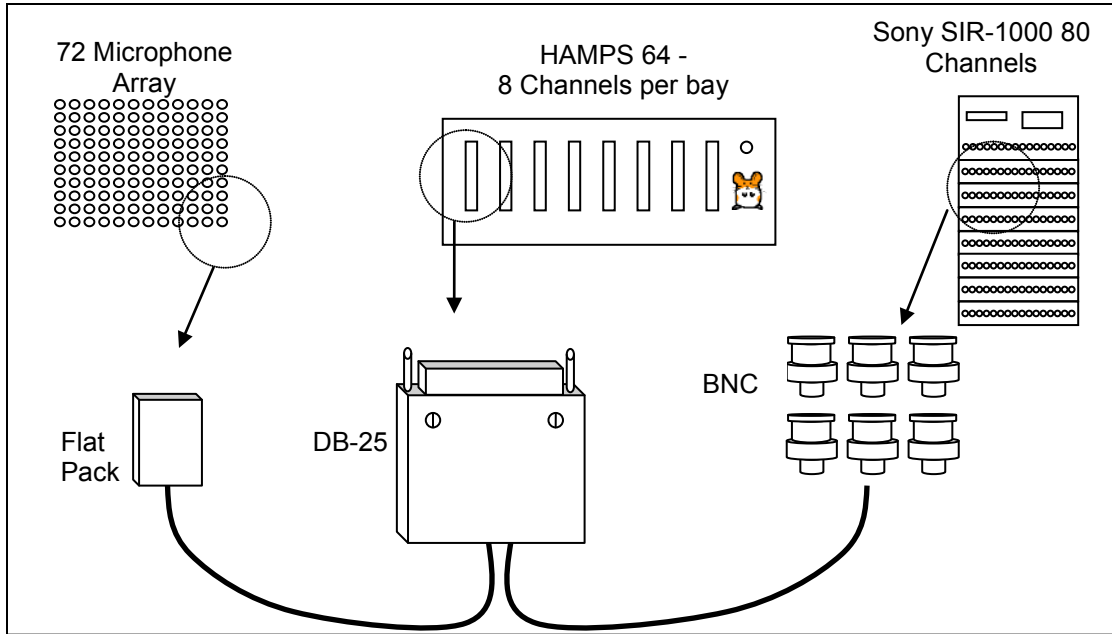
Figure 3.7: Schematic of NAH instrumentation setup

Two minutes of data were recorded at each array position for both random and burst random excitation types. All microphone data acquisition equipment was located in the control room to reduce the chance of noise data contamination. Again, a foam barrier between the amplifier unit and the microphone array was used for the same purpose.

The following four plots are the raw time histories from the NAH data. Shown are the input forces for both the random and burst random data sets, as well as the microphone response at the drive point microphone measurement. It can be seen in the burst random measurements that both the force cell and the microphone levels had decreased to the noise floor prior to the subsequent "burst on" portion of the measurement. This was important to minimize the leakage in the signals.
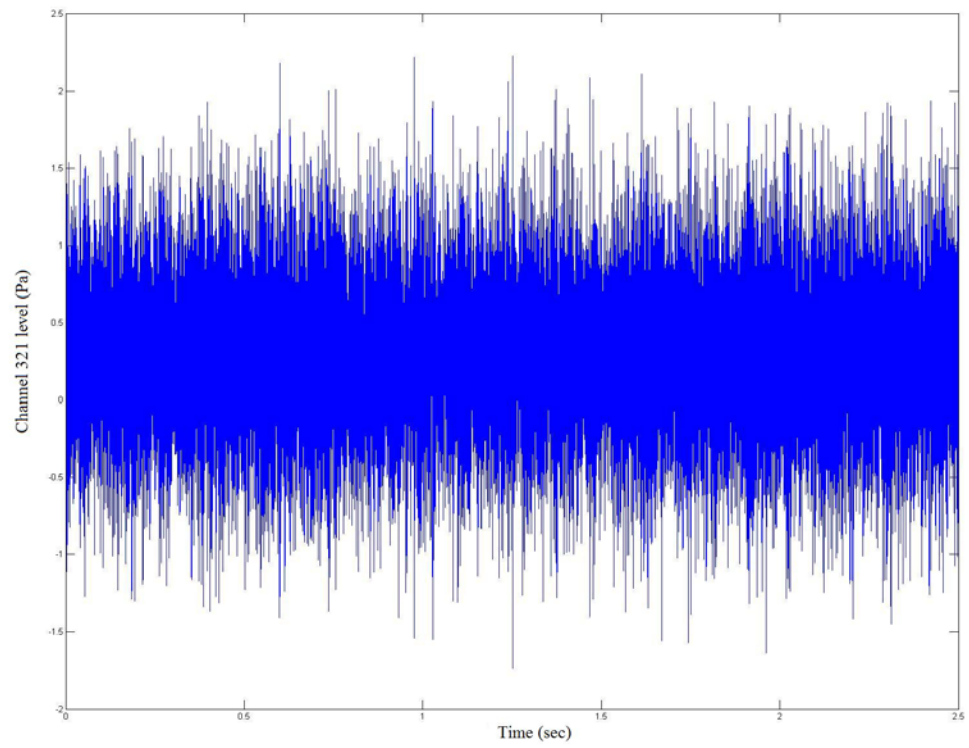
Figure 3.8: Microphone response at Channel 321 for Random Input
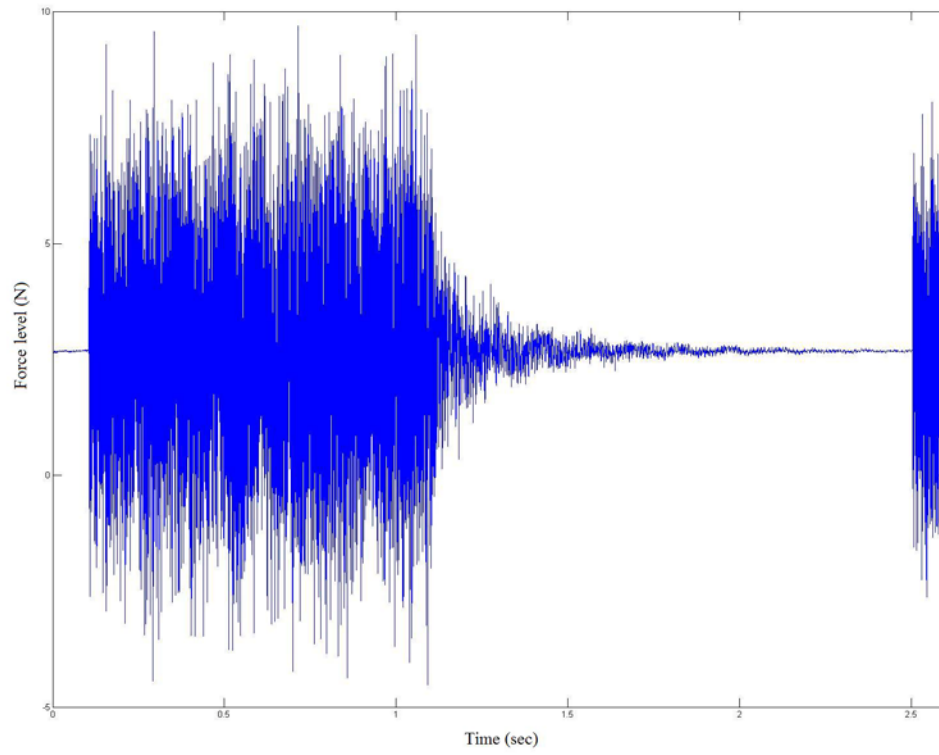
Figure 3.9: Force Cell levels for Random Input
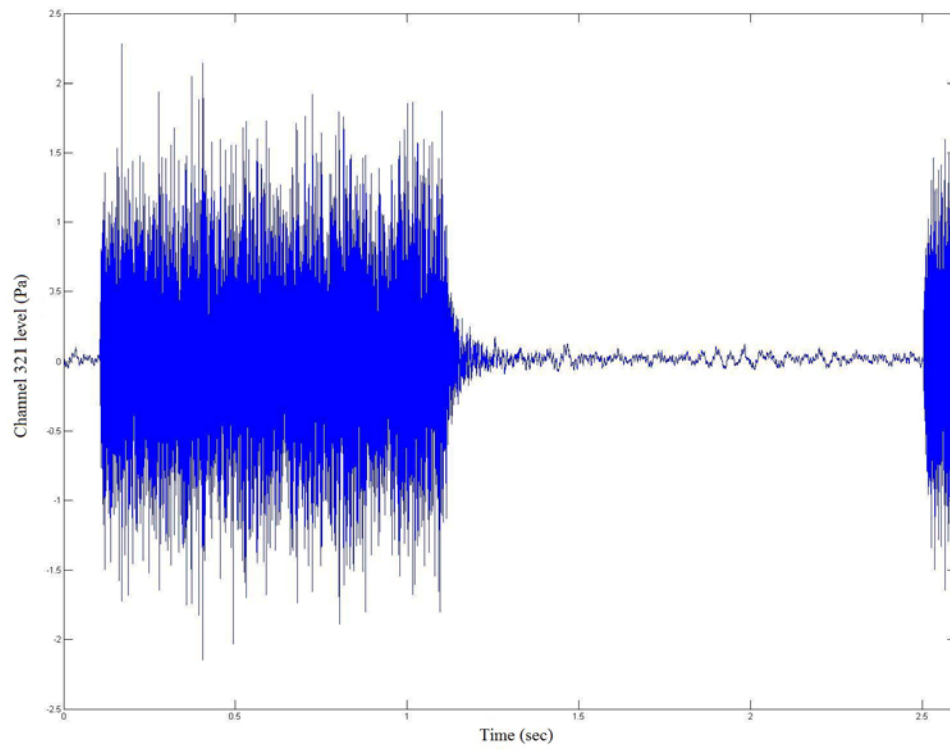
Figure 3.10: Microphone response at Channel 321 for Burst Random Input
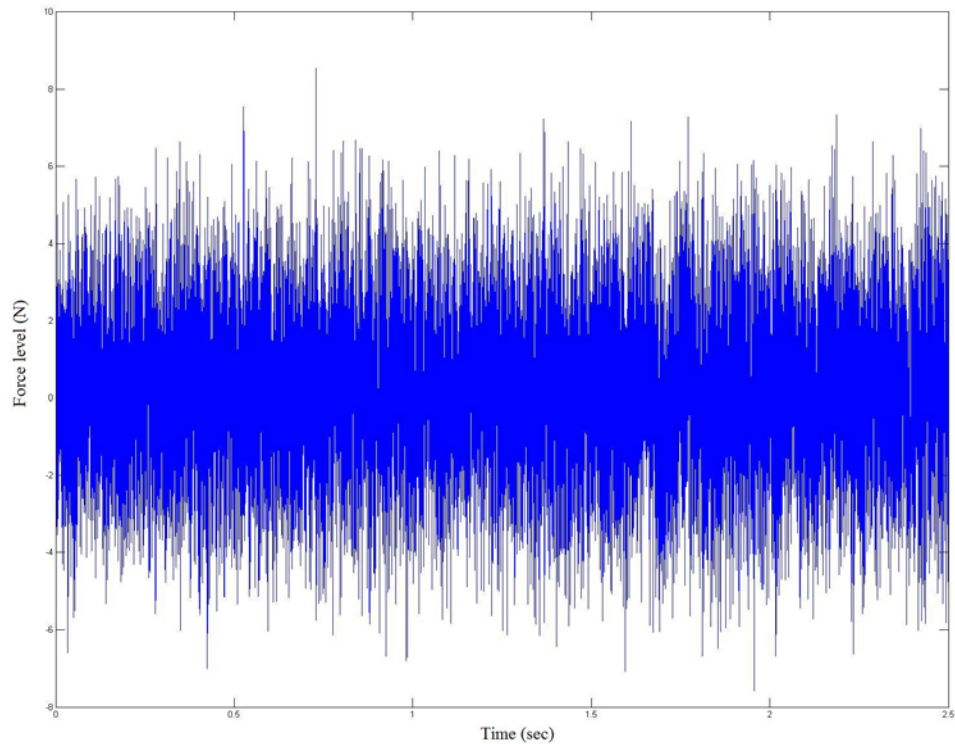
Figure 3.11: Force Cell levels for Burst Random Input

3.2   Experimental Limitations

The laser vibrometer was chosen for the direct measurements instead of accelerometers

because of the mass loading issues that the accelerometers would have created. Multiple

options for accelerometers were considered – adding accels to the entire panel for one

measurement, roving a few accels over multiple measurements, roving a few accels and

dummy masses to keep the mass consistent over multiple measurements – but all of these

options led to mass loading the plate, which was undesirable. When an object is mass

loaded, the dynamics of the system are altered. Adding mass to a system lowers the

resonant frequency, and adds damping – both of which would affect the comparison of

the analytical results with the experimental results. The laser vibrometer proved to be an effective non-contact measurement method.

In this case, a shaker providing random and burst random excitation was used. The random noise was a completely random signal – continuously generating a new sequence of random numbers. The signal was not periodic, requiring the addition of a Hanning window prior to analysis of the data as to reduce leakage. The burst random excitation consisted of 50% on, 50% off for each average. Each burst was a different random signal, which excited the structure slightly differently each time.

For this experiment, single input – multiple output (SIMO) measurements were taken. This was done for ease of experimental setup and data acquisition. A multiple input – multiple output (MIMO) system was also considered, which would have used a second shaker to excite the structure. This second shaker would have also provided random and burst random excitation, but would have been uncorrelated with the first. Benefits to MIMO testing include the ability to put energy into the structure at multiple locations, ensuring that all output points were sufficiently excited and more easily identifying closely coupled modes or repeated roots. It was determined that a single input was sufficient to excite the modes of interest.

3.3 Data Processing

Modal analysis was done using X-Modal version 2.8.4, a software package written by the Structural Dynamics Research Lab at the University of Cincinnati. The laser vibrometer data were saved to universal files, making it possible to import them directly to X-Modal. The NAH data were transferred from the SONY AIT tapes to ".bin" files, allowing the data to be processed using Matlab and ultimately, X-Modal. The Matlab scripts calculated the cross-power matrix between the microphone output and force cell input raw data using a blocksize of 12,000 and no overlap. For the burst measurements, the data were truncated so that 30 burst averages were used at each array point. A uniform window was applied to the data and a wavenumber filter of 0.6 was added to reduce the spatial leakage of the data.

Wavenumber filters were applied to reduce the higher order wavenumber noise in the reconstructed data. For example, an evanescent wave that completes 10 wavelength cycles prior to reaching the microphone (and is decaying exponentially en route) will be reduced close to the noise floor by the time it is measured. Reconstructing the hologram with these evanescent waves included will produce noisy data. Wavenumber filters are chosen so that the majority of the energy is preserved, while the higher order noise is minimized, or filtered out (8). The following plots show the partial pressure data at 288Hz, which is the frequency of the highest mode of interest in this study. As the highest frequency, it will have the most potential for wavenumber noise in the reconstruction. These plots are the first quadrant of the radiation circle, as discussed in chapter 2. The unfiltered wavenumber domain data is shown in Figure 3.12. It can be

seen that most of the energy here (as shown by colors trending towards red) is contained within $k_x = 20$ and $k_y = 15$. This is the energy which needs to be preserved when the wavenumber filter is applied.
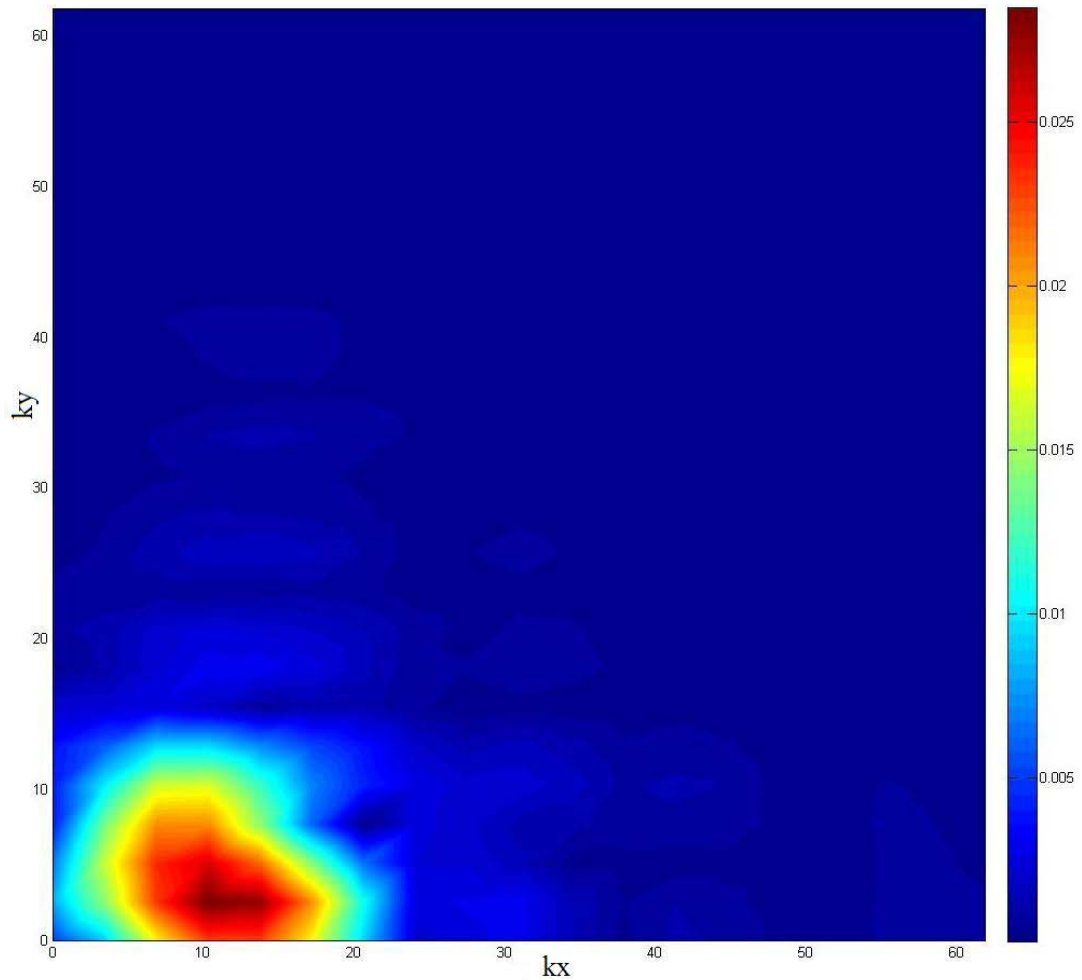
Figure 3.12: Unfiltered Partial Pressure Data (288Hz)

The effect of applying the wavenumber filter of 0.6 to the data is shown in Figure 3.13.
Here it can be seen that the low wavenumber data is still intact, however the higher

41

wavenumber noise is filtered out. This will create a reconstructed hologram with less noise.
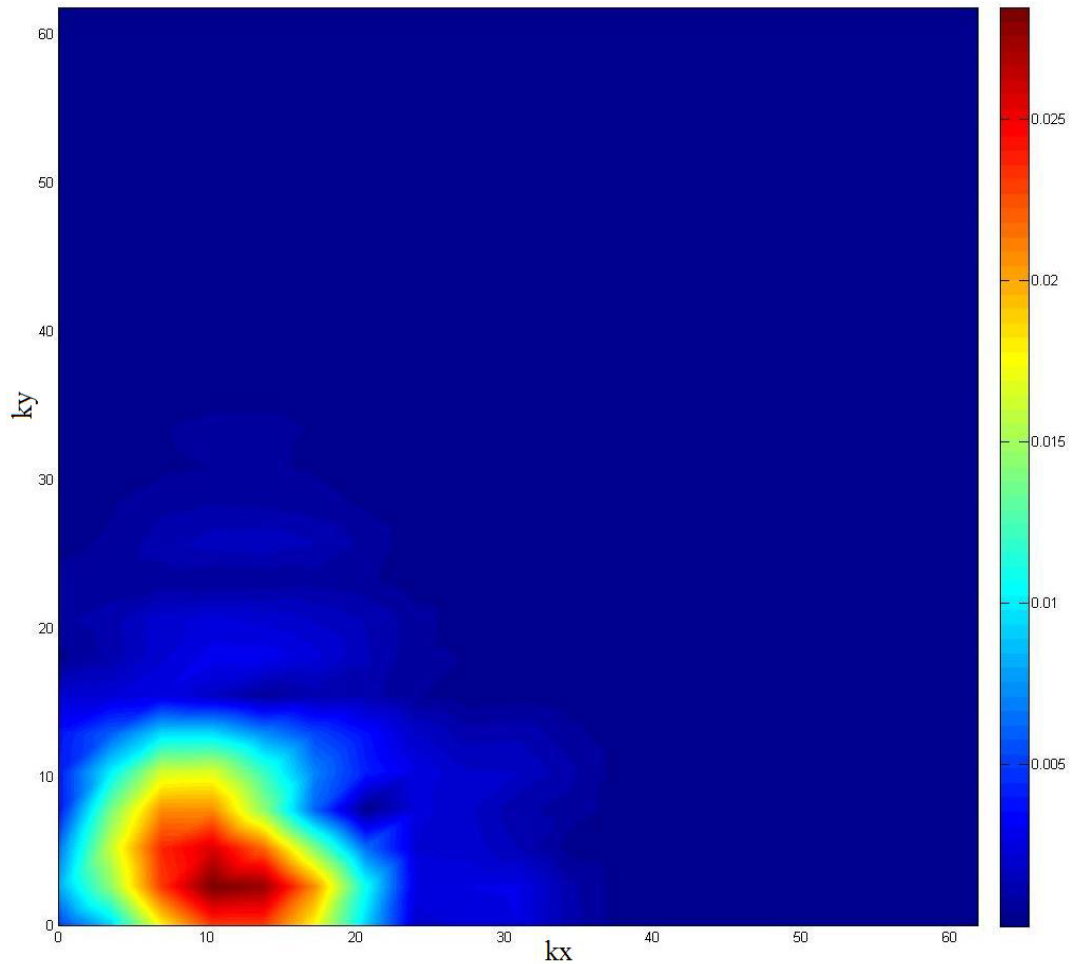
Figure 3.13: Partial Pressure Data (288Hz); Wavenumber Filter of 0.6 Applied.

In contrast to Figure 3.13, data with a wavenumber filter of 0.1 is shown in Figure 3.14. Here it can be seen that a lot of the high energy in the lower wavenumbers is filtered out along with the higher wavenumber noise. This is an undesirable effect, as it reduces the information needed to reconstruct an accurate hologram at the plate surface.
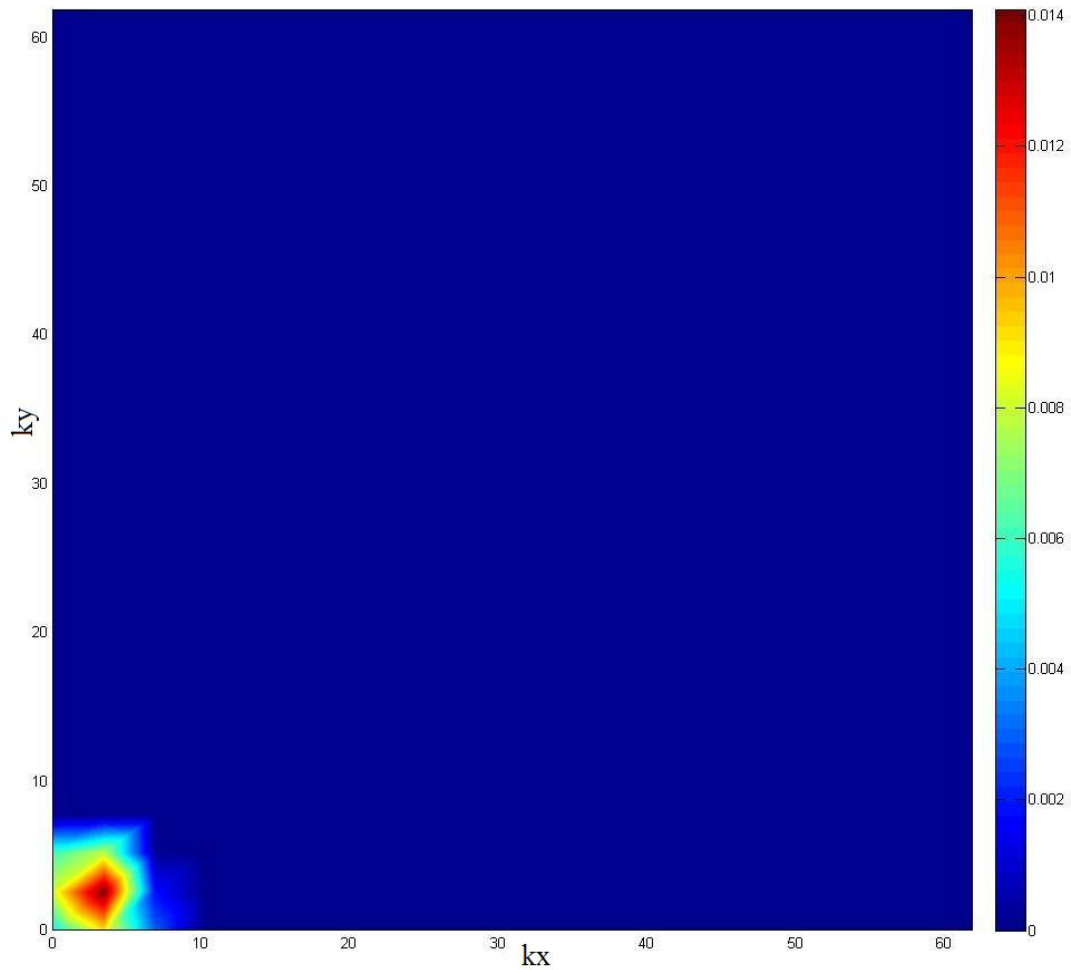
Figure 3.14 Partial Pressure Data (288Hz); Wavenumber Filter of 0.1 Applied.

Once the NAH surface velocity FRF data were in universal file format, they were imported into X-Modal. Parameters in X-Modal were set to analyze the data using the Eigensystem Realization Algorithm (ERA), and employed a start time iteration of 0-15% in steps of 3%. All output locations were used in the calculations. Once the pole results were displayed, each natural frequency and mode shape was examined and one pole chosen from the cluster based on the modal parameters.
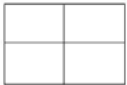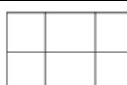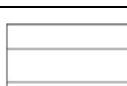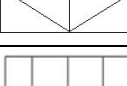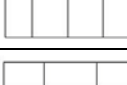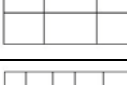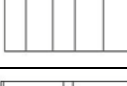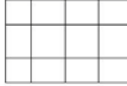
Chapter 4: Results

In this chapter, the results are discussed. The experimental data from the NAH and Laser measurements were compared to an FEA model. Results of all three methods are compared for frequency, damping and mode shape agreement. Both subjective and objective methods are used to determine correlation. Ideally, all three parameters would agree for the modal results would be considered the same.

4.1   Finite Element Model

A model was created in VA-ONE (15), an finite element (FE) modeling software package, using an aluminum plate of size 24 inches by 36 inches by 0.25 inches, representing the x, y, and z directions, respectively, of the physical panel. "Aluminum" is defined in VA-ONE with the following properties: density of 0.0002526 lb-s^2/in^4; tensile modulus of 1.03×10^7 psi; shear modulus of 3.873×10^6 and poisson's ratio of 0.3296 and total mass of 22.5 kg. VA-ONE uses a modified COSMIC Nastran code, a verified NASA developed solver, for its FE analysis, and in this instance, used 7495 quadrilateral FE elements in the process. The boundary conditions for the analysis were free-free-free-free. Surface velocity was predicted and the mode shapes found are shown in Table 4.1.

Table 4.1
FEA Results from Free-Free-Free-Free Analysis

Frequency (Hz)	Shape	Shape Description
37.21		First torsion
40.17		First bending – length-wise
86.13		Second torsion
94.31		First bending – width-wise
107.64		First bi-axial bending
126.65		First torsion + bending
160.13		Third torsion – length-wise
184.05		Fourth torsion
226.65		Third bending – length-wise
253.45		Second bi-axial bending
274.93		Second torsion + bending
275.71		Fifth torsion
282.02		Third torsion – width-wise

4.2   Excitation Analysis

As discussed in chapter 3, the test was set up such that an aluminum plate measuring 24 inches x 36 inches by 0.25 inches (in the x, y, and z directions, respectively) was hung by two bungee cords from a steel stand. The plate was driven with a mechanical shaker in the lower corner (at ([x,y,z] = [24,0,0]) as seen below in Figure 4.1. The plate was driven with both random and burst random excitation. These measurements were compared to determine if leakage would affect the input signal, and subsequently the output measured by the laser and holography arrays. Leakage was a concern in the random measurements because the plate had minimal damping added to it. Energy that fell to the adjacent bins of the lightly damped peaks or the lightly damped anti-resonances would have a significant affect on the outcome of the modal results – primarily in increased damping values. The FRF chosen to analyze was at the input forcing location – between the laser measurement at point 247, and the force cell at the driving point, at the same location. This is illustrated in Figure 4.1.

The data processing parameters were also discussed in chapter 3. In summary, to reduce leakage errors, a Hanning window was applied to the random measurements and the burst random data was burst "on" for 50% of the sample time and "off" for 50% to allow the structure to completely damp out.
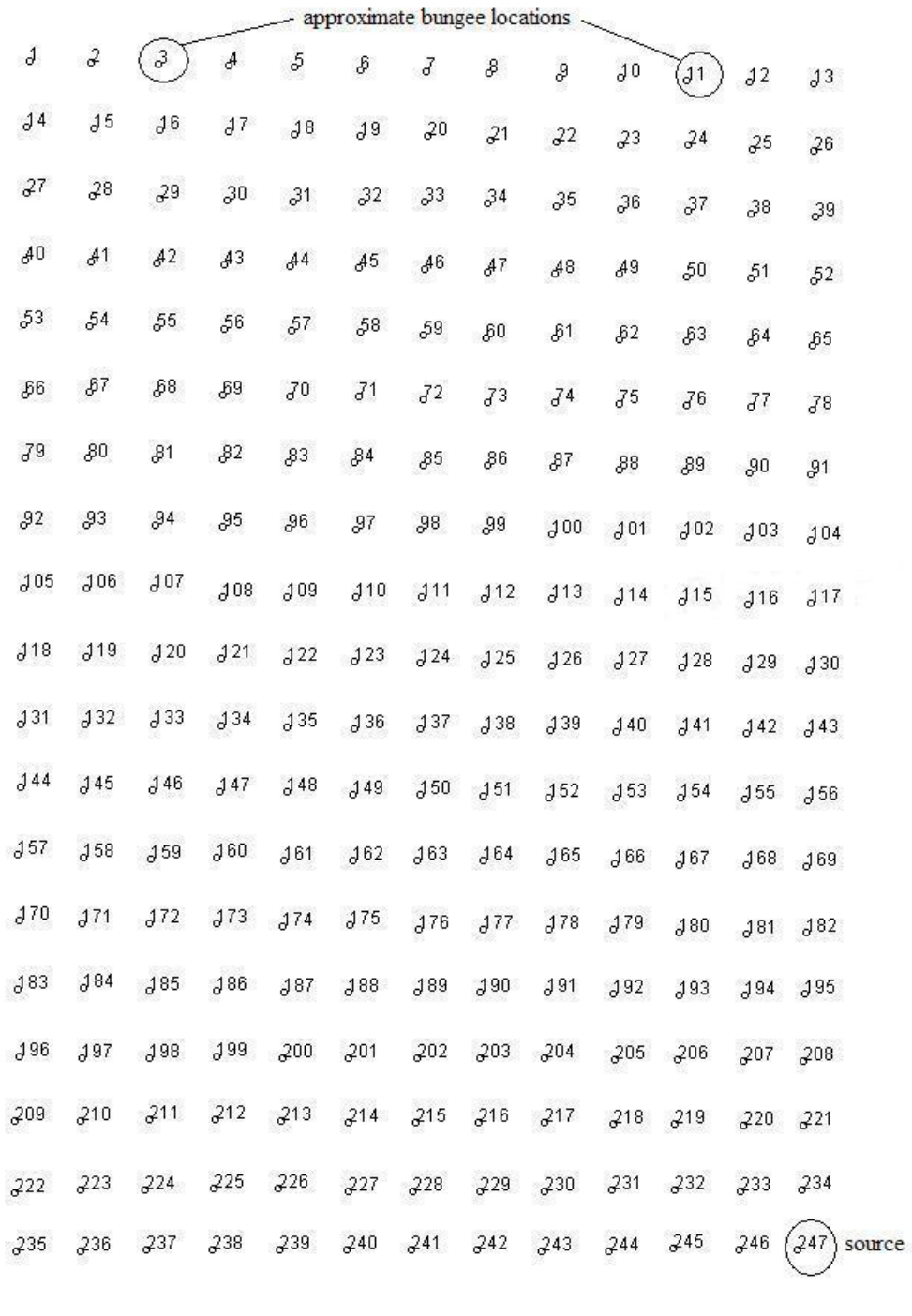
Figure 4.1: Laser Measurement Locations

47

It can be seen in Figure 4.2a that the FRF for each type of excitation shows a lightly damped plate. However, the peak and anti-resonance values are not the same. It can be seen in the peak at 126 Hz that the magnitude of the burst random FRF is nearly twice that of the random FRF. This can be seen to a varying degree at all the peaks and anti-resonances in the plot. These differences are possibly due to a variety of things: the damping of the panel may have been realized at a lower value when it was given the chance to "ring out" unimpeded during the burst measurements, as opposed to the data processing of adding a Hanning window.
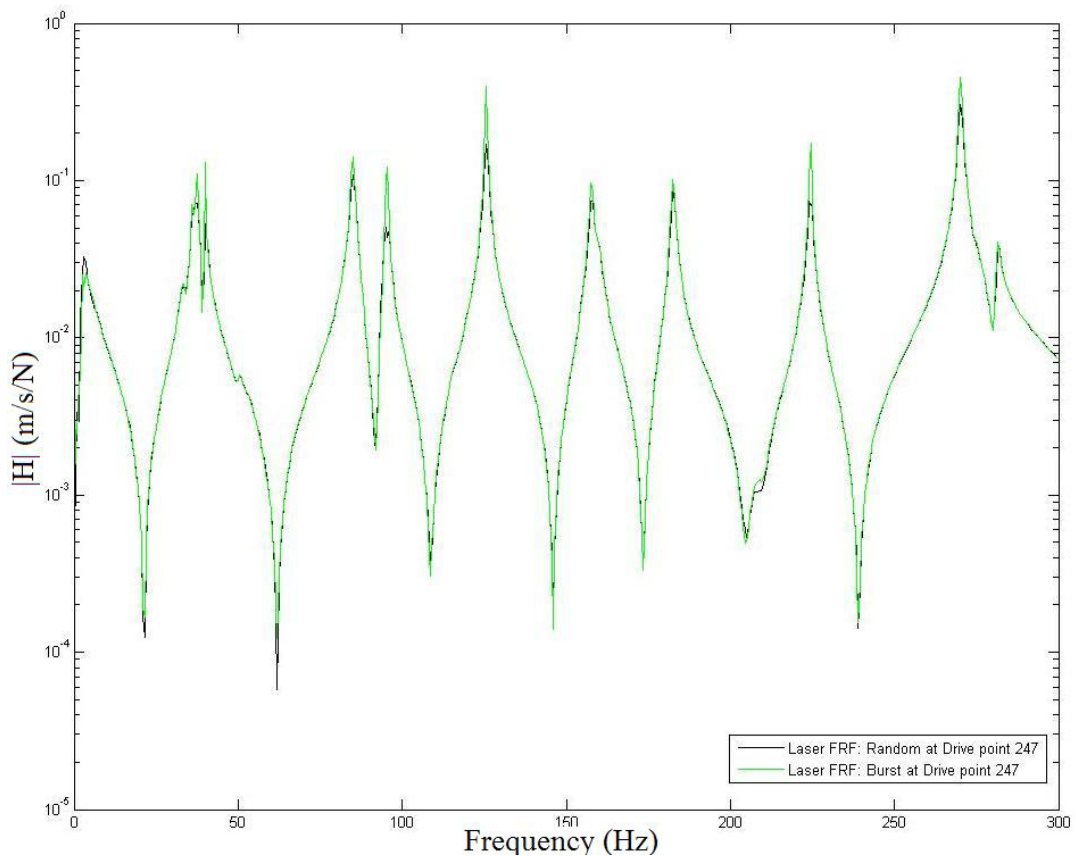
Figure 4.2a: Comparison of Random & Burst Random Laser FRF's.

The differences in the peak levels between the burst and random measurements can be

seen more clearly in Figure 4.2b. Due to these differences, the burst random data will be

analyzed from this point forward.
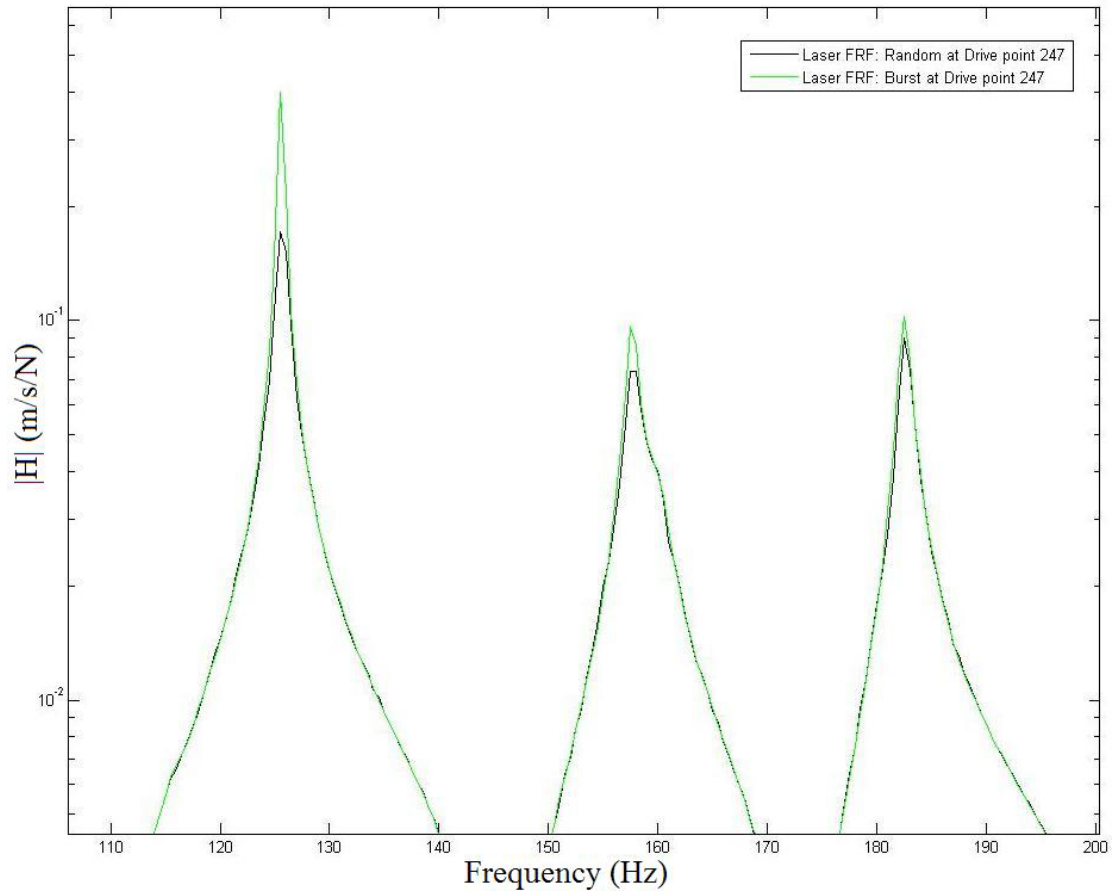
Figure 4.2b: Close Up Comparison of Random and Burst Random Laser FRF's.

The comparison of the NAH random and burst random FRF's can be seen in Figure 4.3.

These data are the sound pressure levels at the microphone compared to the force cell at

the shaker, and not processed through the holography calculations. It can be seen that the

data below approximately 80 Hz is not very clear, which prompted a look into the

49

coherence of the microphones (see Figure 4.4). It can also be seen that during the burst random measurements, there is a 60 Hz tone (and its first harmonic at 120 Hz). The peak and anti-resonance levels are each not identical between data sets; however both have the same mean value and variance.
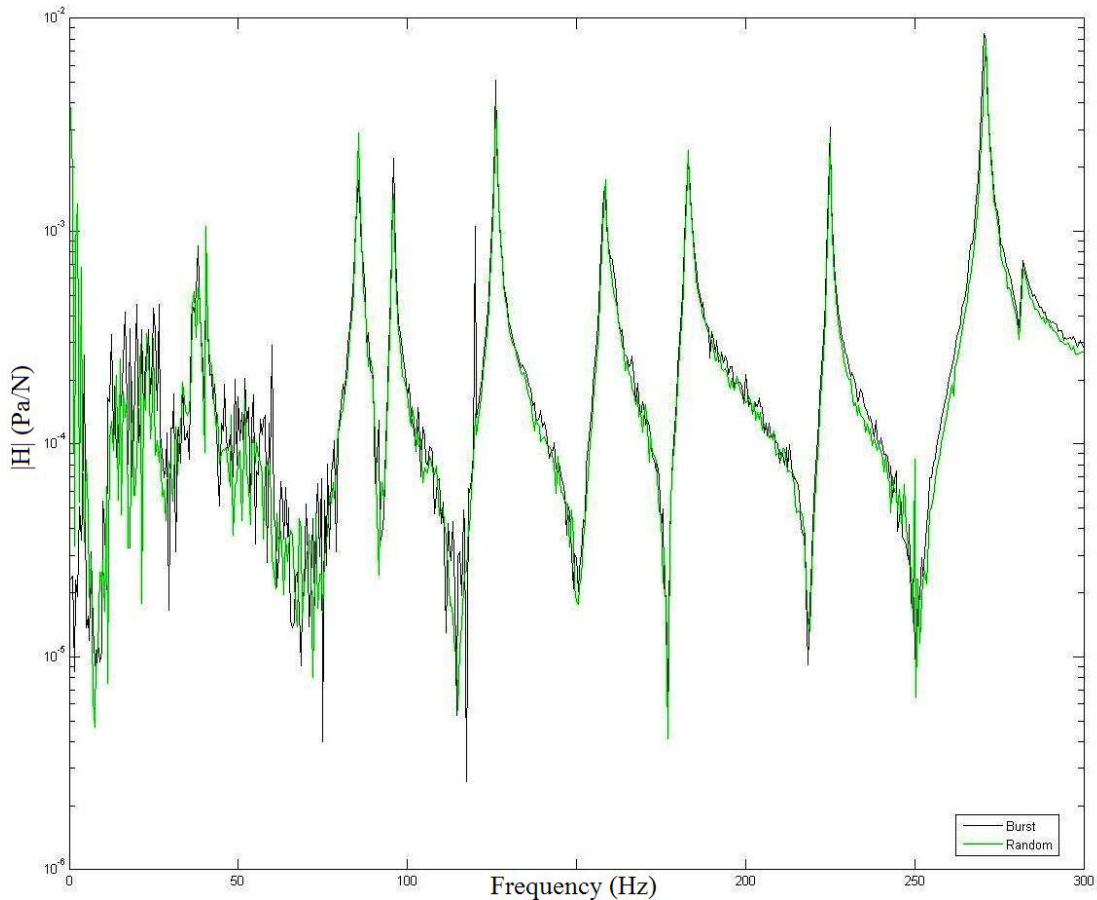
Fig 4.3: Comparison of Random and Burst Random NAH "FRF's" at Microphone Array

As previously mentioned, the microphone coherence was investigated to determine if it was the cause of the poor data quality below 80 Hz. The data from the drive point microphone (point 247 in Figure 4.1) from the burst random data is plotted below in Figure 4.4. It can be seen that indeed the microphone coherence is low below 80 Hz,

which will produce poor quality FRF data in that frequency range. The ideal coherence is at 1, and the values approach that for each resonant frequency of the calculated FRF's, even at 38 Hz and 40 Hz. The dips in the coherence in Figure 4.4 correspond to the anti-resonances of the microphone FRF in Figure 4.3. Since the frequencies of interest (resonant frequencies) have high coherence, the data is acceptable. The low coherence is a product of the microphones, not of the data or the processing.
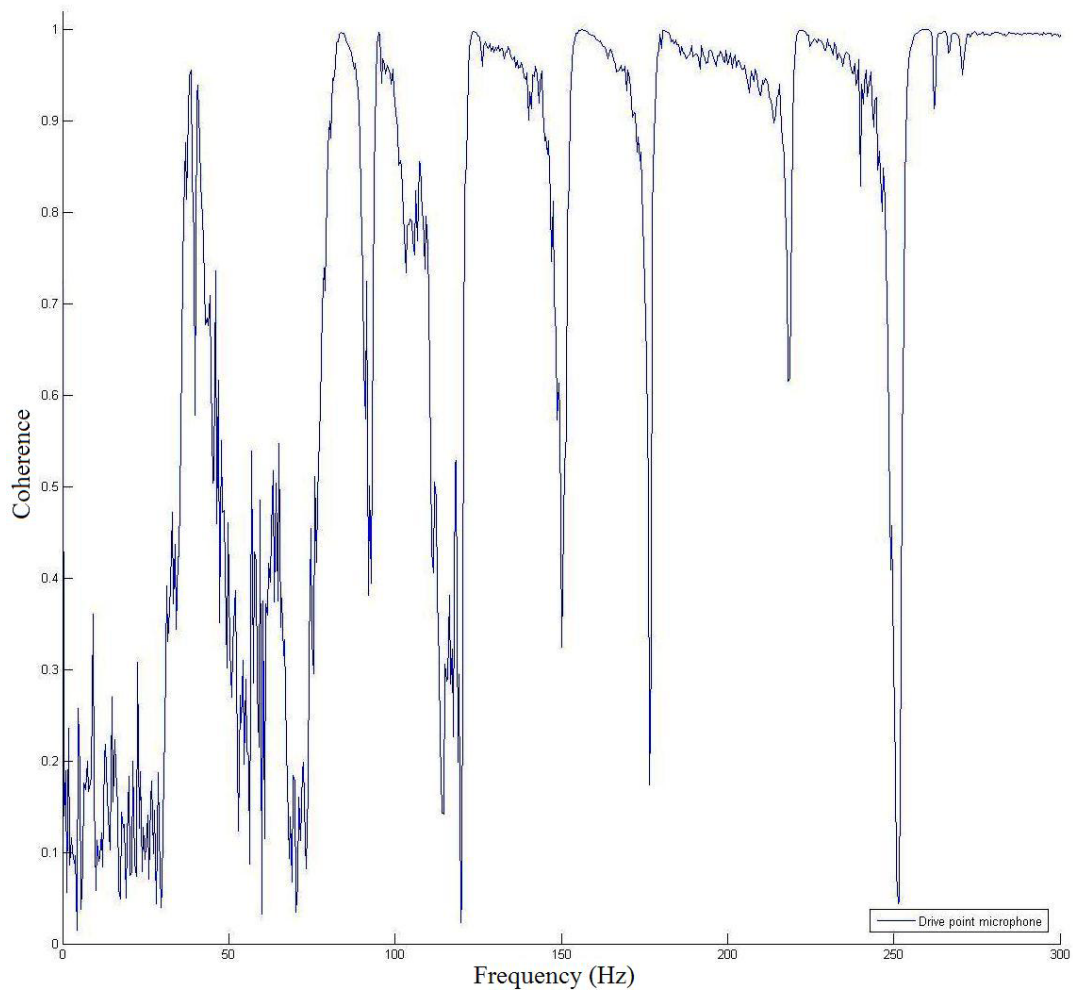
Figure 4.4: Coherence at Drive Point Microphone

Figures 4.5a and 4.5b show that the input autopower for each of the six scan positions of

the NAH microphone measurements, as well as the average input autopower (in black).

It can be seen that all six are nearly identical, with insufficient differences between them.

It can be said that all six inputs are the same, creating six nearly identical cases for

analysis.
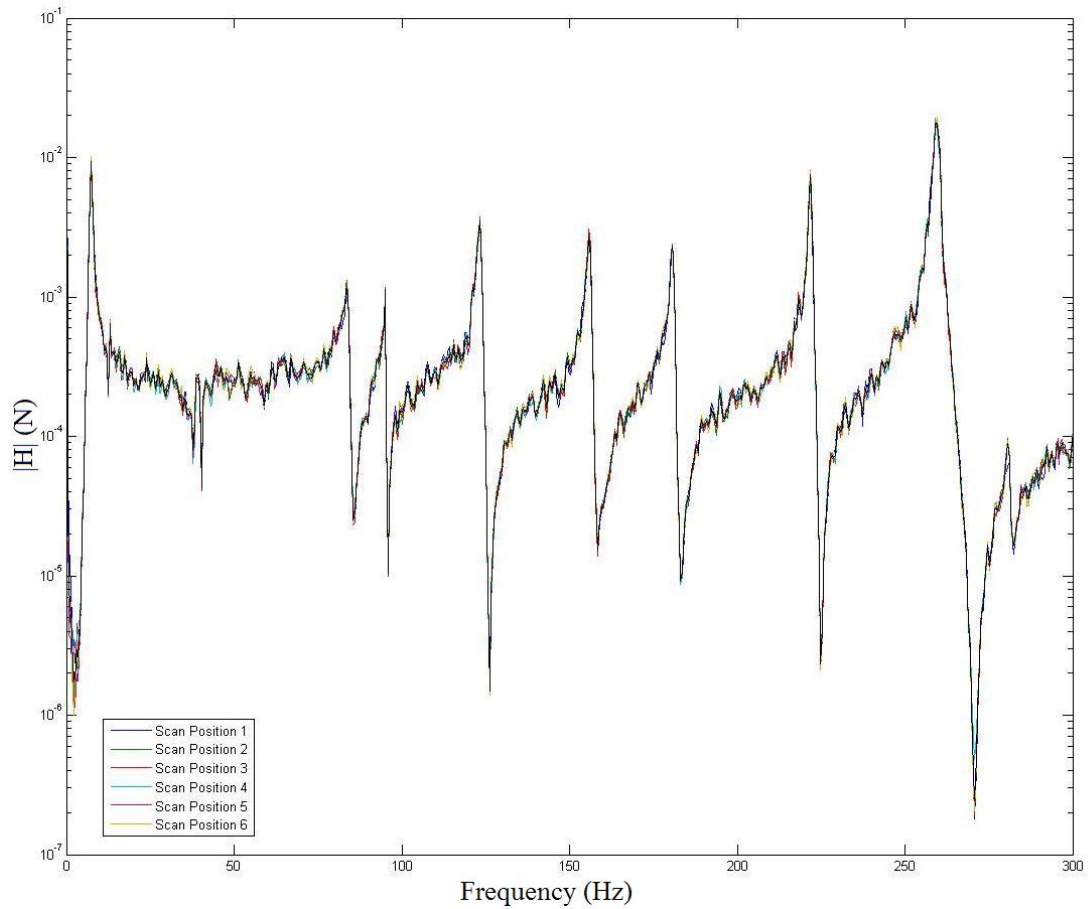
Figure 4.5a Input Autopower for NAH Microphone Measurements
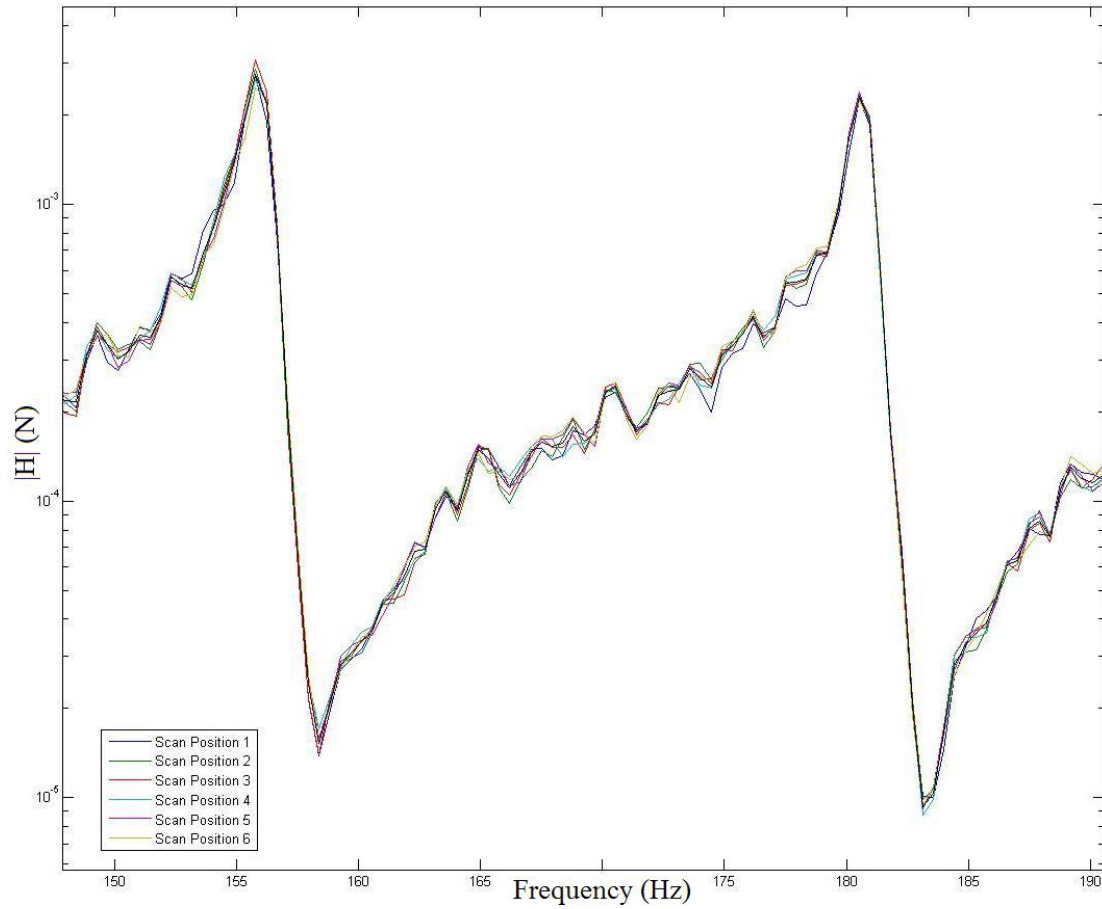
Figure 4.5b: Input Autopower for NAH Microphone Measurements, Zoomed in

The input autopower was also compared between the Laser measurements and the NAH

measurements and the results are shown in Figure 4.6.
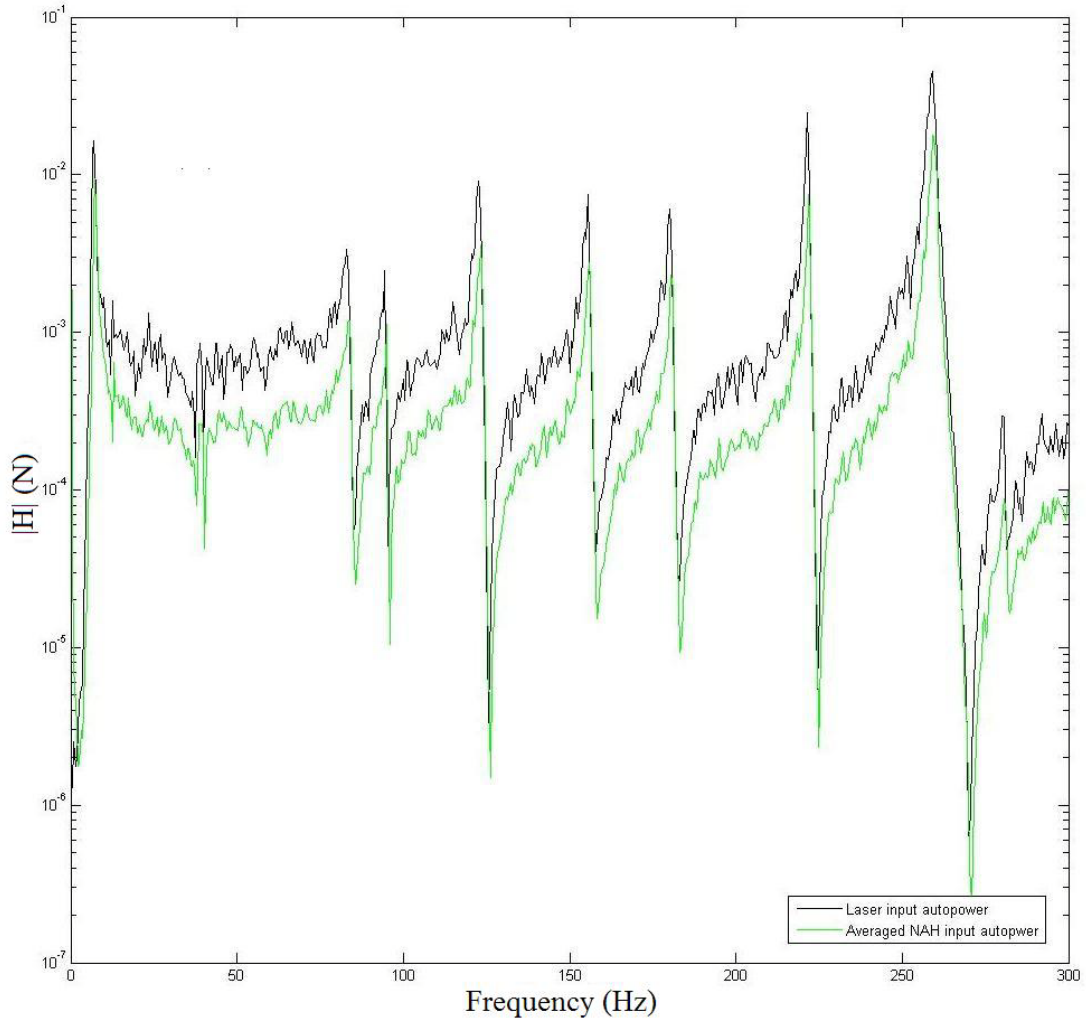
Figure 4.6: Comparison of Laser and NAH Input Autopower

An important fact to remember is that the constructed frequency domain data at the

hologram surface is not an actual FRF; that is, it is not a measured response normalized

to the input force. The "FRF" of the NAH measurements is actually the reconstructed

velocity at the surface, which has been divided by the input autopower from the force

cell. This "pseudo FRF" is compared to the actual FRF from the laser in Figure 4.7a

below and will be used in the modal analysis. Shown here are the surface velocity of the

Laser and the reconstructed surface velocity of the NAH measurements, both normalized
to their respective input autopower data.
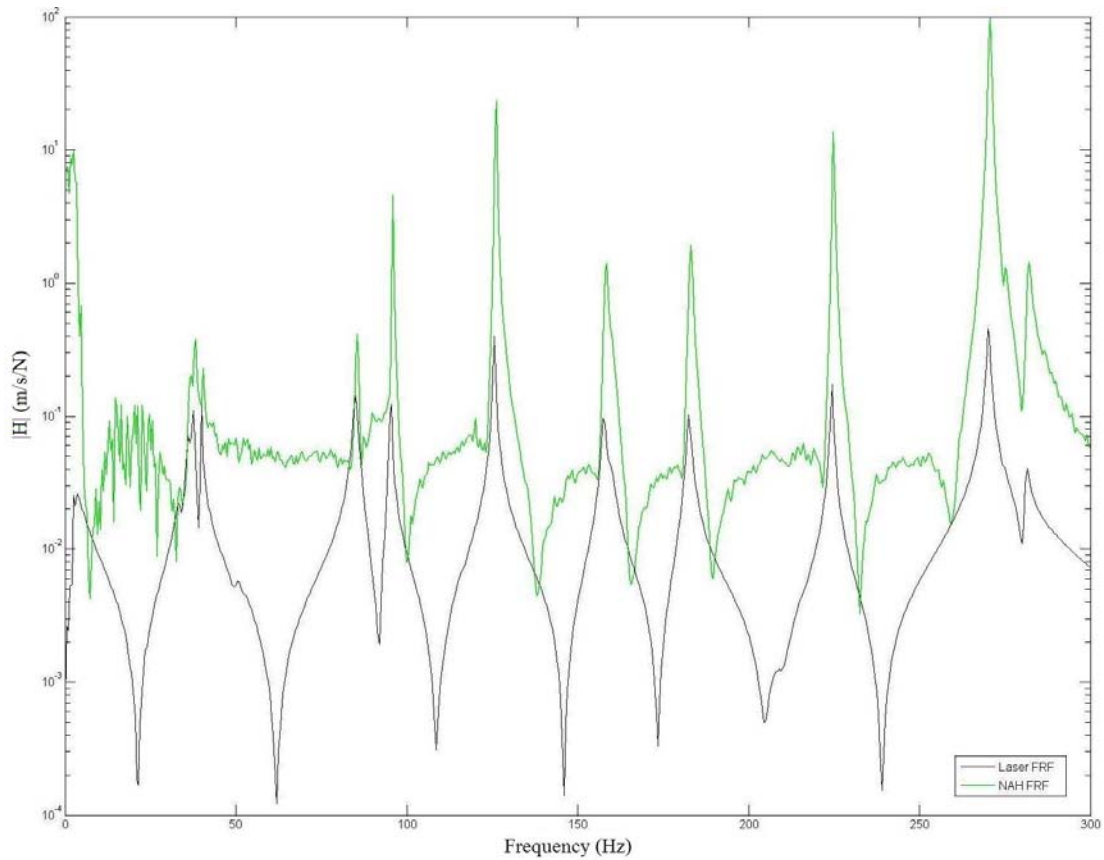
Figure 4.7a: Laser FRF & NAH "FRF" at Drive Point

It can be seen in Figure 4.7a that there are significant differences between the two
measurements. The frequency peaks are within 1.5 Hz, but do not line up exactly. This
is potentially due to the air coupling between the plate and the microphones. There is a
discrepancy in the magnitudes of the two measurements, which is believed to be a scaling
issue with the NAH processing, however the exact reason is unknown. The NAH "FRF"
does not have sharp anti-resonances, but instead produced broadband "noise" between the

frequency peaks. These were thought to be an artifact of the NAH processing, and likely

a product of the calculated data approaching the noise floor of the reconstruction,

however, as seen in Figure 4.7b, an "FRF" comparison at point 219, the broadband

"noise" between peaks does not exist. This will be discussed further when the mode

shapes are addressed.
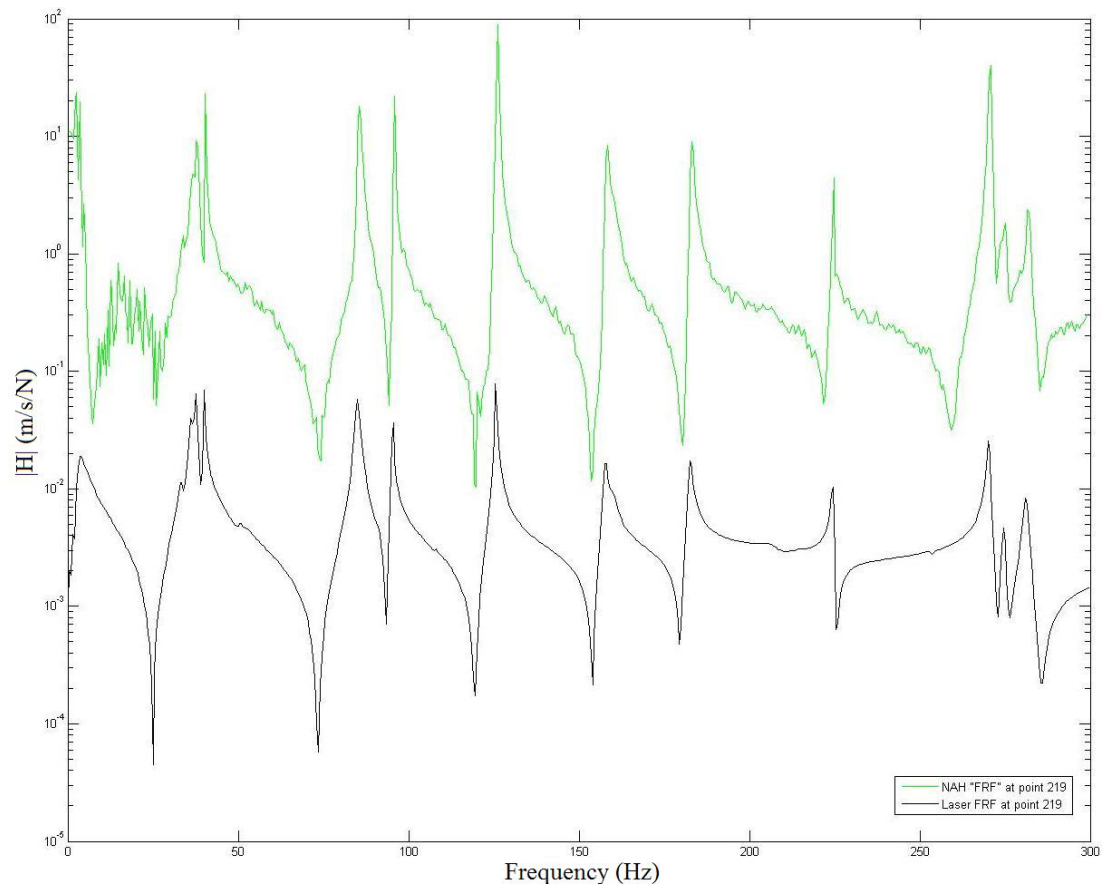
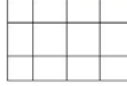Figure 4.7b: Laser FRF & NAH "FRF" at Measurement Location 219
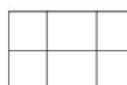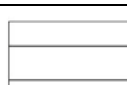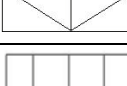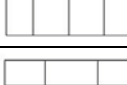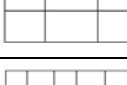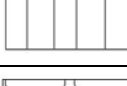
It is expected that these two FRF measurements will not produce identical modal analysis

results due to the differences seen here.

4.3   Modal Analysis

The modal parameter estimation was performed using the ERA time domain method, as discussed in chapter 3. The natural frequencies found from both the Laser and NAH systems were compared to the FE analysis. The frequency results can be seen in Table 4.2 below. It can be seen that the frequencies are very close across all methods. The FEA model natural frequency results agree with both the Laser and NAH measurements within 2%.

Table 4.2
Comparison of Frequency Results

Mode #	Laser (Hz)	NAH (Hz)	FEA (Hz)	Shape	Shape Description
1	37.71	37.45	37.21		First torsion
2	40.36	40.41	40.17		First bending – length-wise
3	85.62	85.48	86.13		Second torsion
4	95.88	95.78	94.31		First bending – width-wise
5	108.05	108.21	107.64		First bi-axial bending
6	126.17	126.12	126.65		First torsion + bending
7	158.43	158.32	160.13		Third torsion – length-wise
8	183.12	182.91	184.05		Fourth torsion
9	224.9	224.89	226.65		Third bending – length-wise
10	254.58	253.71	253.45		Second bi-axial bending
11	270.72	270.69	274.93		Second torsion + bending
12	273.52	274.79	275.71		Fifth torsion
13	280.78	281.62	282.02		Third torsion – width-wise

It can be seen that the frequency values are within 1 Hz across all methods for the majority of the modes. The 11th mode (second torsion + bending) has a difference of over 4 Hz between the experimental values and the FEA value. As expected, he FEA results were consistently higher than either the laser or NAH estimates. However, with less than 2% difference between methods, it can be said that they all agree.

Figures 4.8 and 4.9 show mean phase colinearity (MPC) plots are shown for the Laser and NAH burst random measurements. It is expected that the estimated mode shapes approach a mathematical ideal of normal modes, or in this case, a straight line. The MPC has a value between 0 (randomly phased vector) and 1 (normal vector). The closer the MPC value is to 0, the more complex the mode is and the closer the value is to 1, the more normal the mode is. Real world structures are by no means ideal, however highly complex modes are usually the result of a faulty modal model (14). In this case, the angle of the line has no bearing on the overall MPC value, however the scatter within each plot does; that is, the more scatter, the lower the MPC value, and the less reliable the mode estimate is. The axes on these MPC plots show the real part of the pole on the x-axis and the imaginary part on the y-axis, as labeled in the bottom left plot of each set.
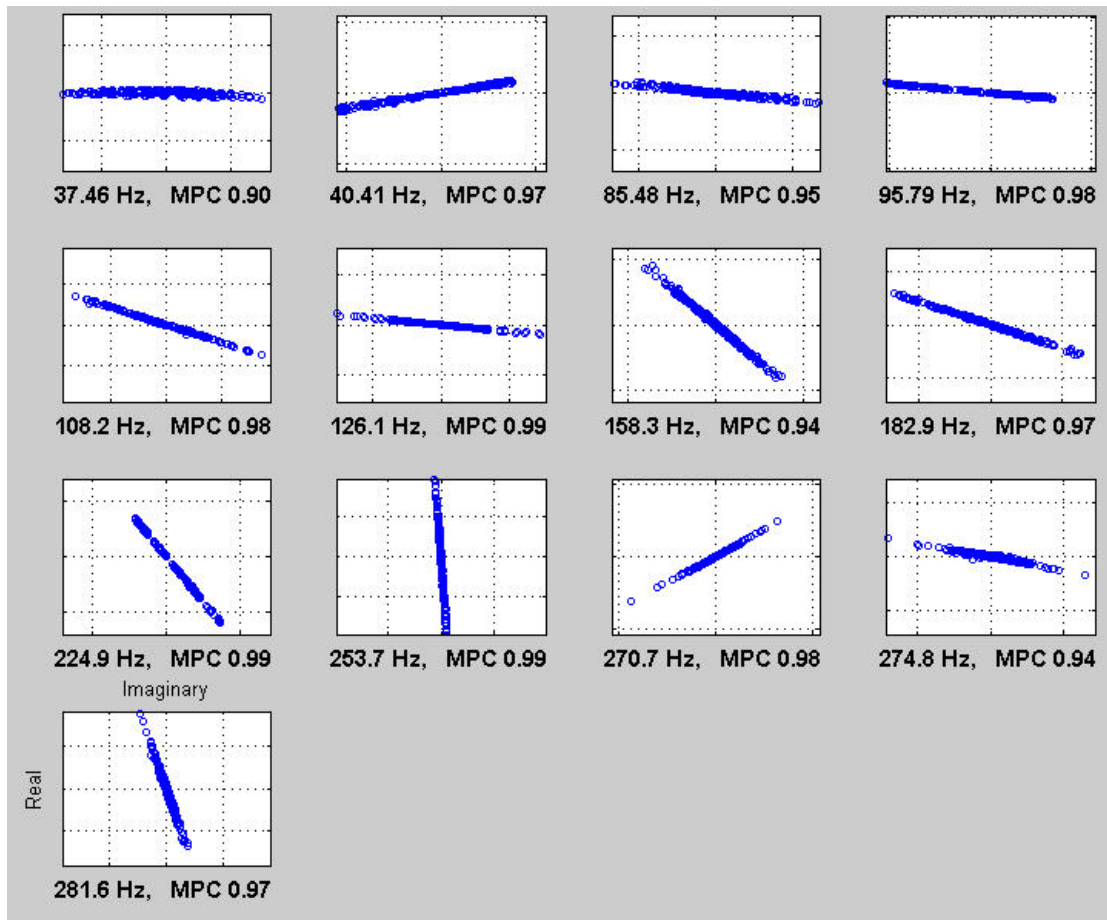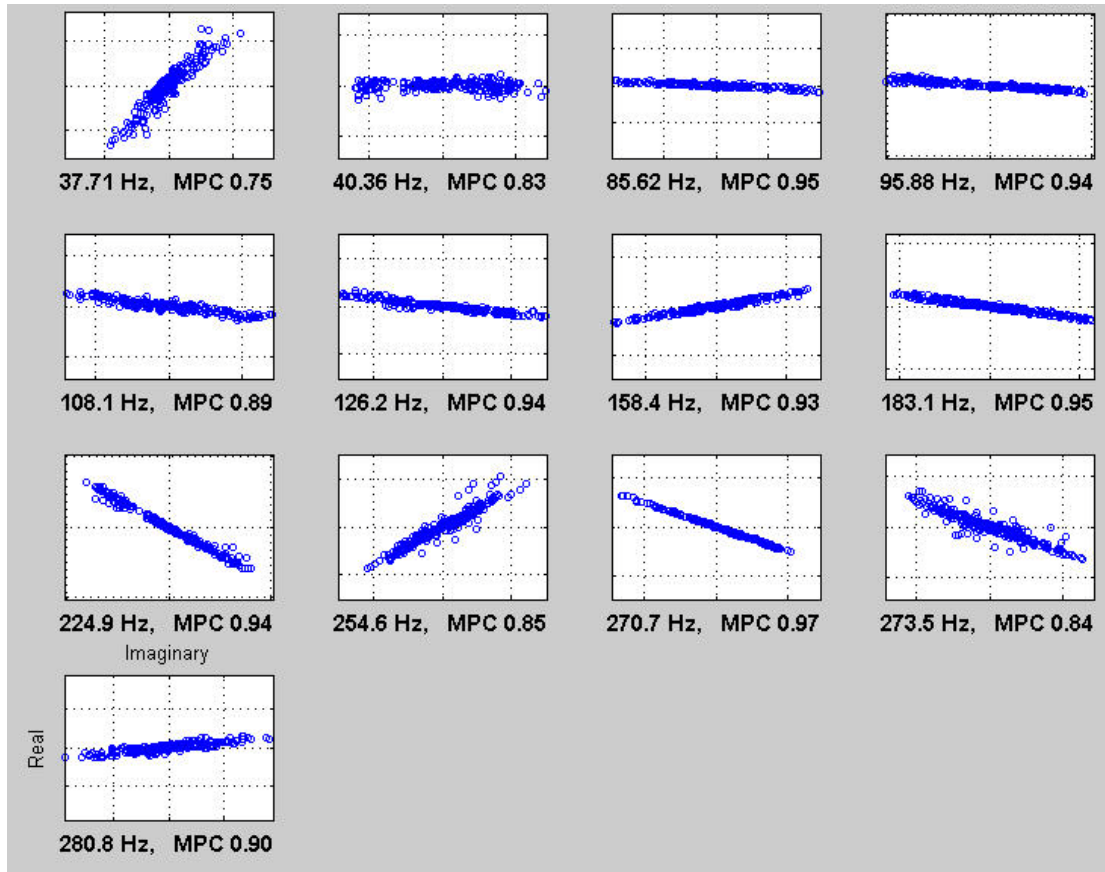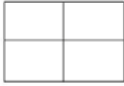
Fig 4.8: Laser Mean Phase Colinearity
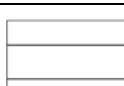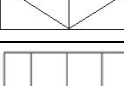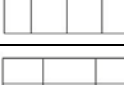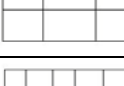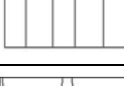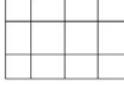
Fig 4.9: NAH Mean Phase Colinearity

It can be seen that the majority of the modes have an excellent MPC value, which is to say that the values are greater than 0.90. The lowest MPC value is the first mode of the NAH measurements, which at 0.75 is still acceptable. The low values for the first two modes of the NAH measurements are indicative of the poor microphone coherence below 80 Hz.

The damping values from each method were compared and have been tabulated in Table 4.3.

Table 4.3

Comparison of Damping Results

Mode #	Laser (% zeta)	NAH (% zeta)	Shape	Shape Description	Difference in Damping (%)*
1	1.275	1.368		First torsion	6.79
2	0.22	0.103		First bending – length-wise	53.18
3	0.576	0.327		Second torsion	43.23
4	0.169	0.068		First bending – width-wise	59.76
5	0.106	0.123		First bi-axial bending	13.82
6	0.167	0.058		First torsion + bending	65.26
7	0.503	0.239		Third torsion – length-wise	52.48
8	0.282	0.144		Fourth torsion	48.93
9	0.111	0.04		Third bending – length-wise	63.96
10	0.174	0.17		Second bi-axial bending	2.29
11	0.133	0.063		Second torsion + bending	52.63
12	0.195	0.068		Fifth torsion	65.12
13	0.226	0.094		Third torsion – width-wise	58.41

*Damping difference was calculated by [Laser – NAH]/Laser

It can be seen that the laser measurements produced higher damping values for 11 of the 13 modes. For the first torsion mode, the difference is only 7%, however the higher modes have a difference of up to 65% (first torsion + bending, fifth torsion). Based on the shapes and levels of the FRF's analyzed, these results are expected. Since the NAH data had higher magnitude FRF values, as well as sharper peaks, it was expected to produce lower damping values.

The mode shapes were compared both qualitatively and quantitatively. The quantitative analysis was done using Modal Assurance Criterion (MAC). The MAC is a mathematical measure of the similarity of the mode shapes. The mode shapes are compared with the following equation:

$$MAC(\{\psi\}_r, \{\psi\}_s) = \frac{\left| \{\psi\}_r^{*t}, \{\psi\}_s \right|^2}{(\{\psi\}_r^{*t}, \{\psi\}_r)(\{\psi\}_s^{*t}, \{\psi\}_s)} \qquad (4.1)$$

If the mode shape vectors, $\{\psi\}_r$ and $\{\psi\}_s$ are the same, then the MAC will be one (13).

Below the Auto-MAC for both the Laser modes and NAH modes can be seen in Fig 4.9 and Fig 4.10, respectively. Figure 4.11 illustrates the quantitative comparison between the Laser and NAH modes.

It can be seen in Figures 4.10 and 4.11 that the auto-MAC of each set of modes compares the MAC value of each mode against itself. From this, it can be determined that there are

no duplicate modes in the analysis and that the conjugate pairs are well matched - indicating that the modes are well estimated.
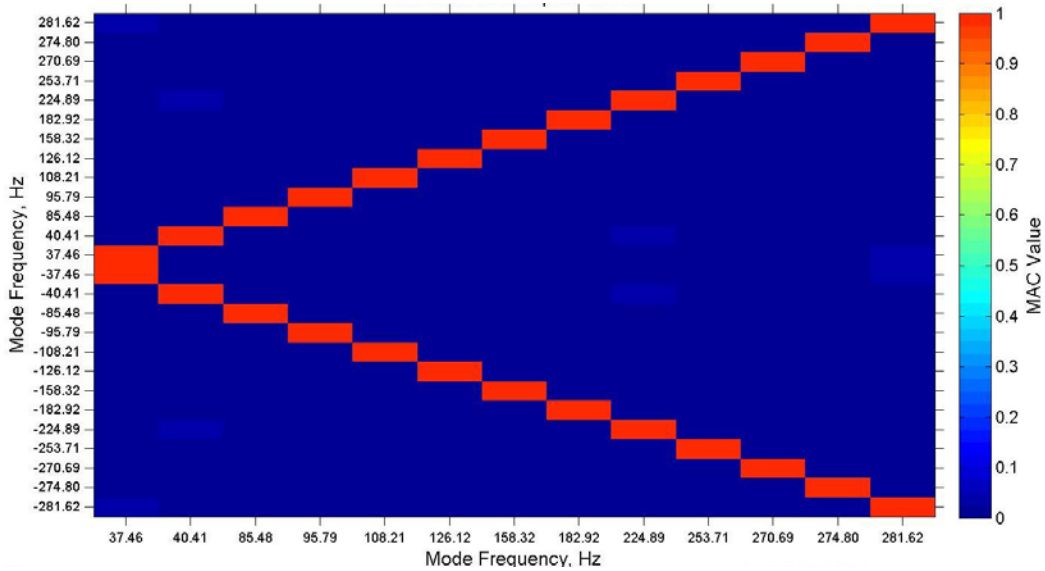

Fig 4.10 Laser Auto-MAC

Figure 4.11 shows a MAC value of 0.67 between the 11th & 12th modes (second torsion + bending & fifth torsion), indicating that the shapes are similar and the modes not well separated.
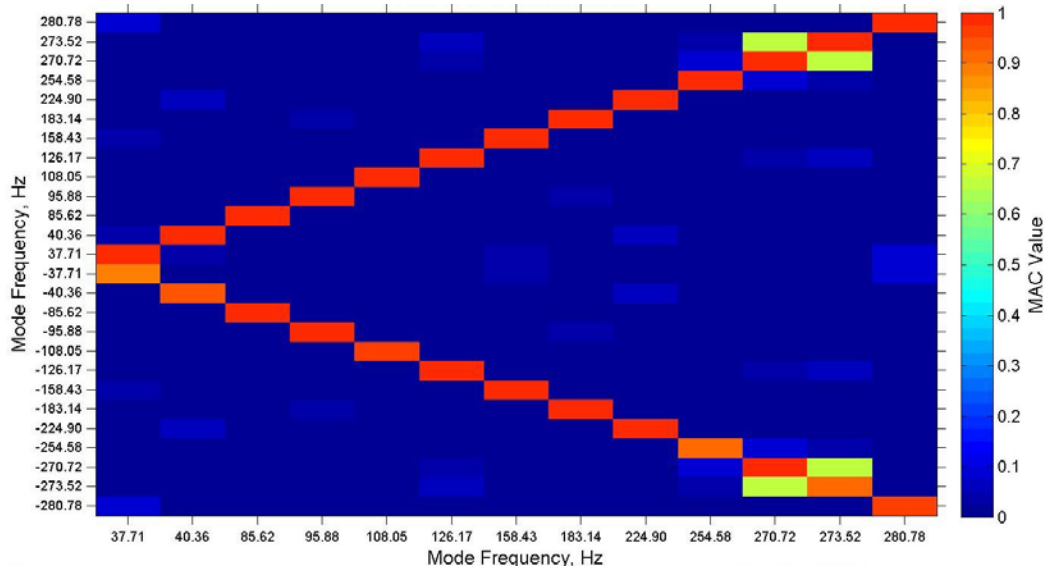
Fig 4.11 NAH Auto-MAC

The mode shapes were then compared against each other. The result is shown in Figure 4.12.
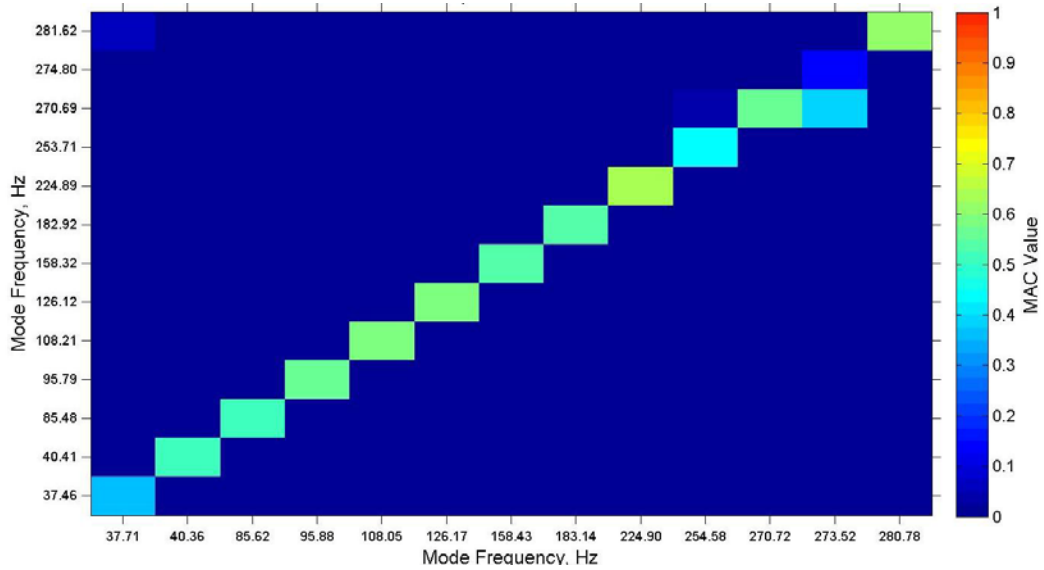

Fig 4.12 Laser & NAH Cross-MAC

It can be seen in Figure 4.12 that the mode shapes appear to be poorly correlated. The

MAC values are around 0.5, which would indicate that the shapes do not agree well. A

visual inspection of each of the shapes in motion revealed that the outer perimeter of data

points in the NAH measurements had motion that was not detectable. The outer

perimeter of both measurements was removed and the shapes compared again. The

results are shown in Figure 4.13.
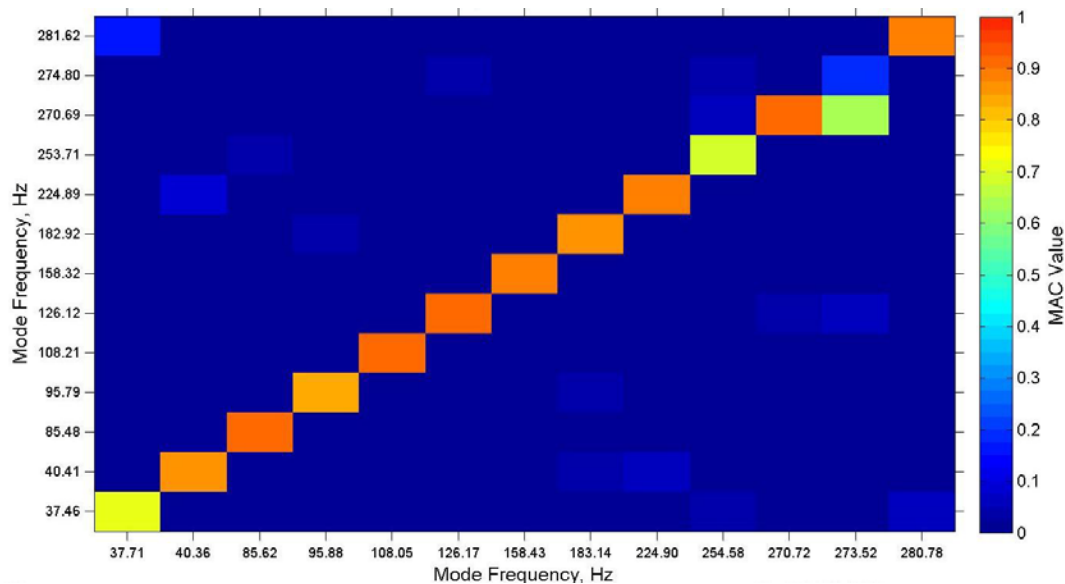
Figure 4.13: Laser & NAH Cross-MAC, outer perimeter removed

It can be seen in Figure 4.13 that when the perimeter is omitted, the shapes agree well.

The MAC values are on the order of 0.85 or higher for 10 of the 14 modes. The first

mode (first torsion) has a MAC value of 0.71, which is a product the lower MPC value of

the NAH estimate of that mode. The 12th mode (fifth torsion) was also not estimated well

for the NAH measurements, and is only a fair match to the laser estimate. It has a MAC

value of 0.63 with the previous mode (second torsion + bending), and 0.18 with its laser counterpart. Referring back to Figure 4.11, it can be seen that the 12th & 13th modes in the NAH estimates had overlap that produced an auto-MAC value of 0.70. The 11th mode (2nd bi-axial bending) also has a lower MAC value (0.69). The MPC value for this from the NAH estimation was 0.85. Looking at the FRF's for each method, it can be seen that this mode was not well excited, which would also account for the lower cross-MAC value.

Mode estimates were also compared using the Polyreference Time Domain (PTD) method. The following MAC results are for the NAH and laser shapes with the outer perimeter of both measurements removed, as in Figure 4.13. The results are shown below in Figure 4.14:
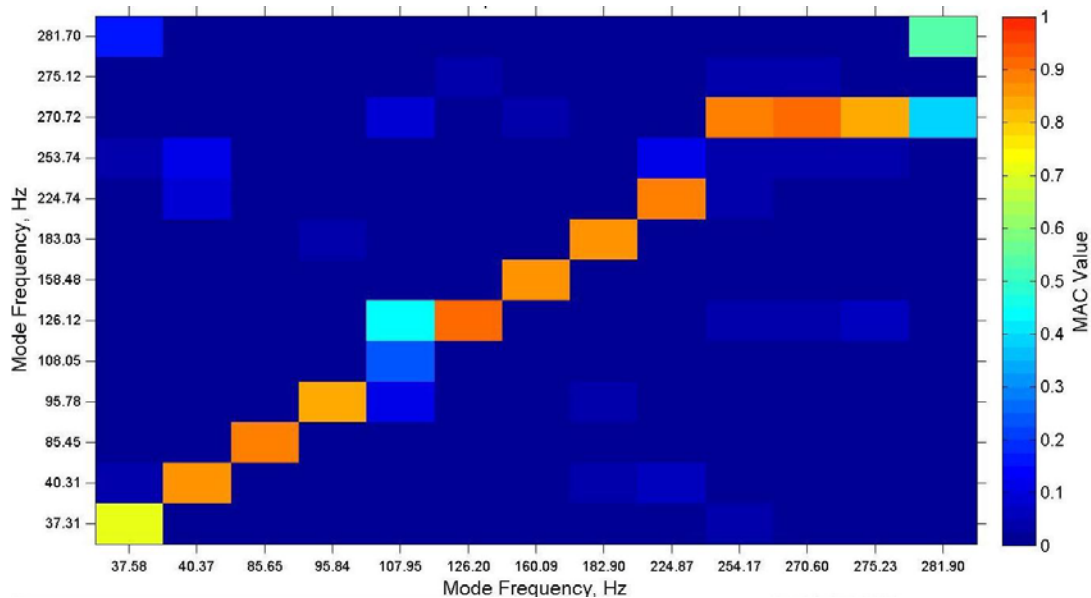

Fig 4.14: Laser & NAH Cross-MAC, outer perimeter removed, PTD method

It can be seen here that the shapes do not compare as well using this method as they did with ERA. While the MAC values of similar mode shapes are comparable to those of the ERA method, the mode estimation did not identify all modes for each measurement method. The MAC value is again low (0.7) for the first torsion mode at ~37Hz, which is similar to the ERA estimate, and due to a low MPC value of the shape itself. The 5th mode (first bi-axial bending), while similar in frequency, does not have a matching shape between the two methods, as seen with the MAC value below 0.5. The higher order modes shapes of the NAH measurements (254.17Hz, 270.6Hz, 275.23Hz) all appear to have the same shape as the second torsion + bending mode estimated for the laser. Although both measurement techniques produced 13 mode shapes for comparison, the agreement between the two is not high. The remainder of the discussion will be based on the mode shapes found using the ERA estimation.

The edge effect seen here, and which is shown below in the mode shape visualizations, was also seen in the FRF's as shown in Figure 4.7. The broadband "noise" on point 247 (drive point in lower left corner) was not an artifact of the NAH processing methods, but a physical phenomenon of the microphone measuring the edge of the plate. It is likely that even though the microphone was in the near field of the plate, the sound pressure from the plate was not high enough to drive the microphone, and was lost in the negative z-plane behind the plate (away from the microphone array). Comparing points 247 and 219 in the mode shapes, it can be seen that point 247 has minimal motion, while point 219 is fully participating in the mode shapes. Therefore, for the comparison analysis

68

(MAC), the data of the perimeter of the plate is removed. This is an inherent limitation to the NAH modal analysis method.

A MAC comparison was done between the FEA results and the experimental results. Figure 4.15 shows the results between the FEA and the Laser results:
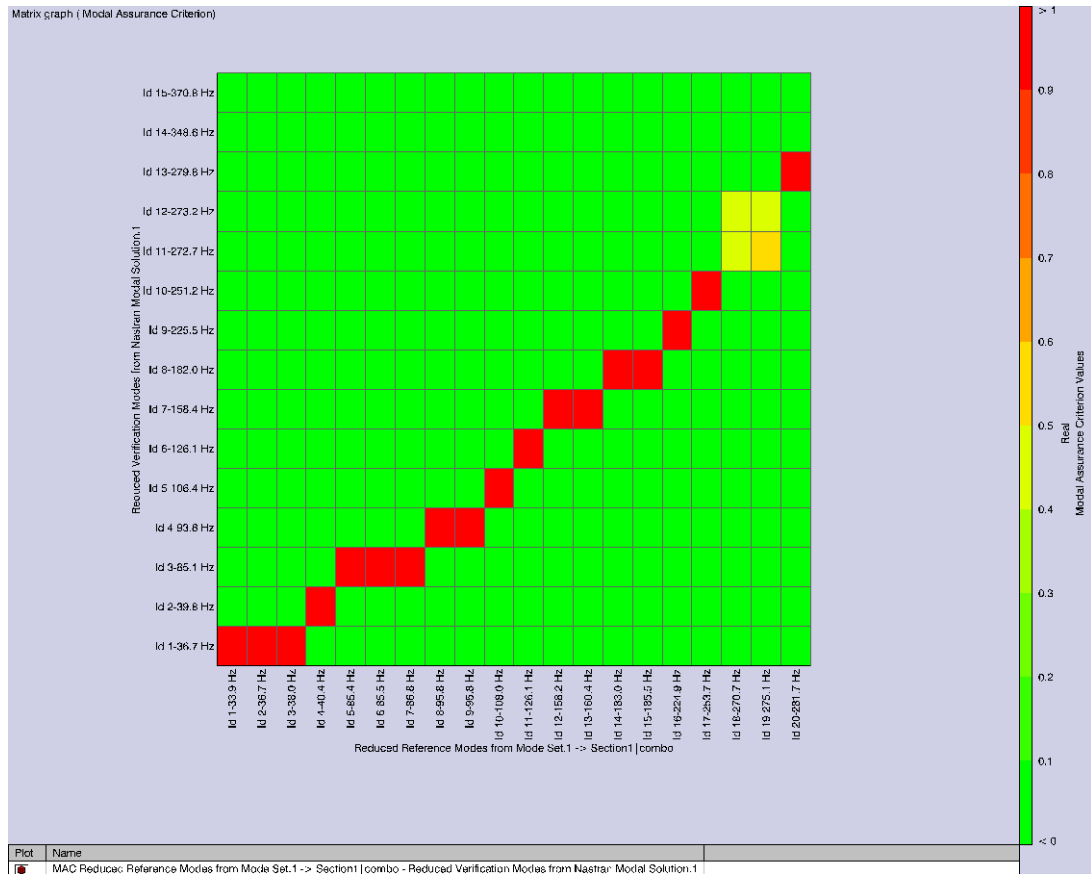

Figure 4.15: Laser (x-axis) and FEA (y-axis) Cross-MAC

It can be seen here that the results are all above 0.90. It can also be seen that the modal parameter estimation (MPE) identified more than one mode shape vector that was well correlated to a specific experimental laser mode shape vector. For example, the first

three Laser mode shape vectors all agree well with the first FEA mode shape vector. The

MPE identified modes from the structure itself (i.e. bungee cords, steel bars) that the FEA

did not predict. This also holds true for the 3rd, 4th, 7th and 8th FEA mode shape vectors.

The 11th and 12th modes were not well identified by the parameter estimation, as can be

seen by the MAC values under 0.5.

Figure 4.16 shows the MAC results between the FEA and experimental NAH parameter
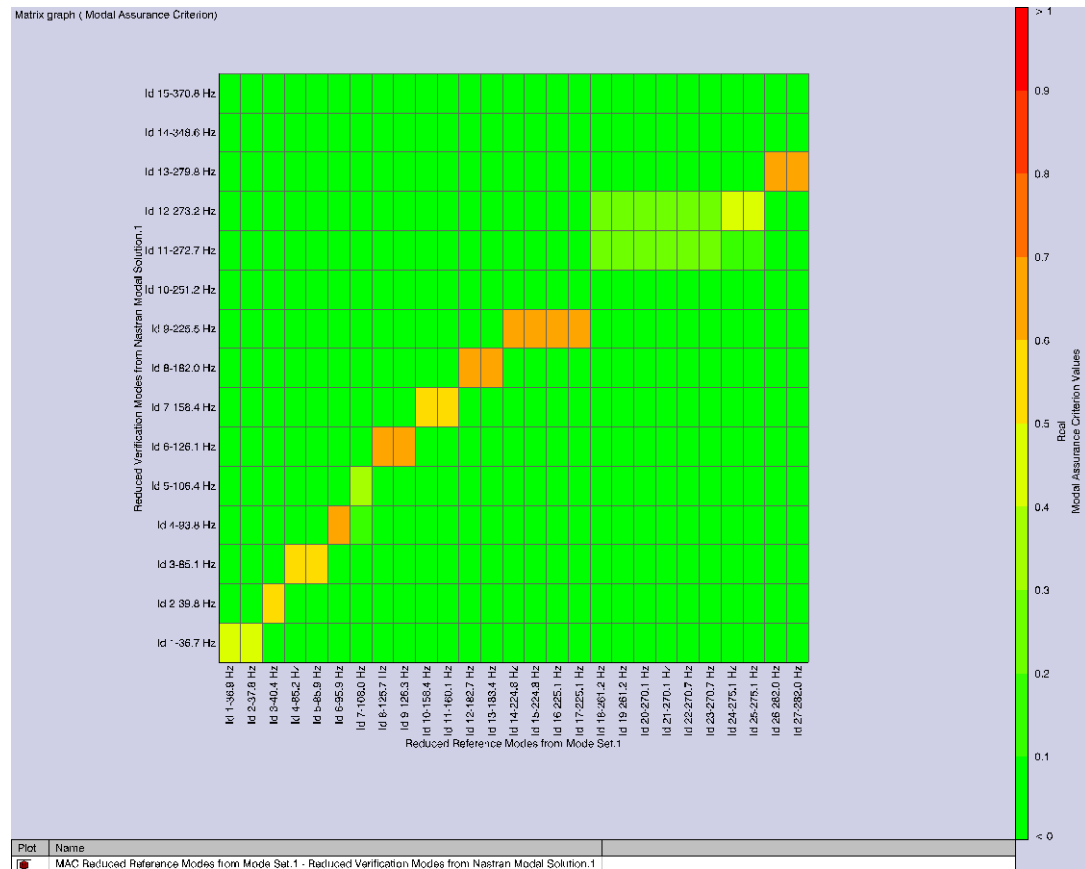
estimation:

Figure 4.16: NAH (x-axis) and FEA (y-axis) Cross-MAC

This comparison was completed with all points included in the geometry (i.e. not removing the outer perimeter). As in the case of the Laser and NAH MAC results, the MAC between the FEA and experimental NAH mode shape vectors do not agree well. The values are all less than 0.7, and the 5th, 10th and 11th modes show values below 0.3. It can also be seen that the NAH parameter estimation, like the Laser, identified modes that were not predicted by the FEA.

A MAC Contribution analysis was done for the FEA/NAH case in which DOF points were removed from the comparison and a new MAC value calculated until the MAC value reached a desired threshold. This provided a quantitative view of the edge effects. Figure 4.17 shows the MAC Contribution bar graph for the first mode (torsion at 37 Hz).
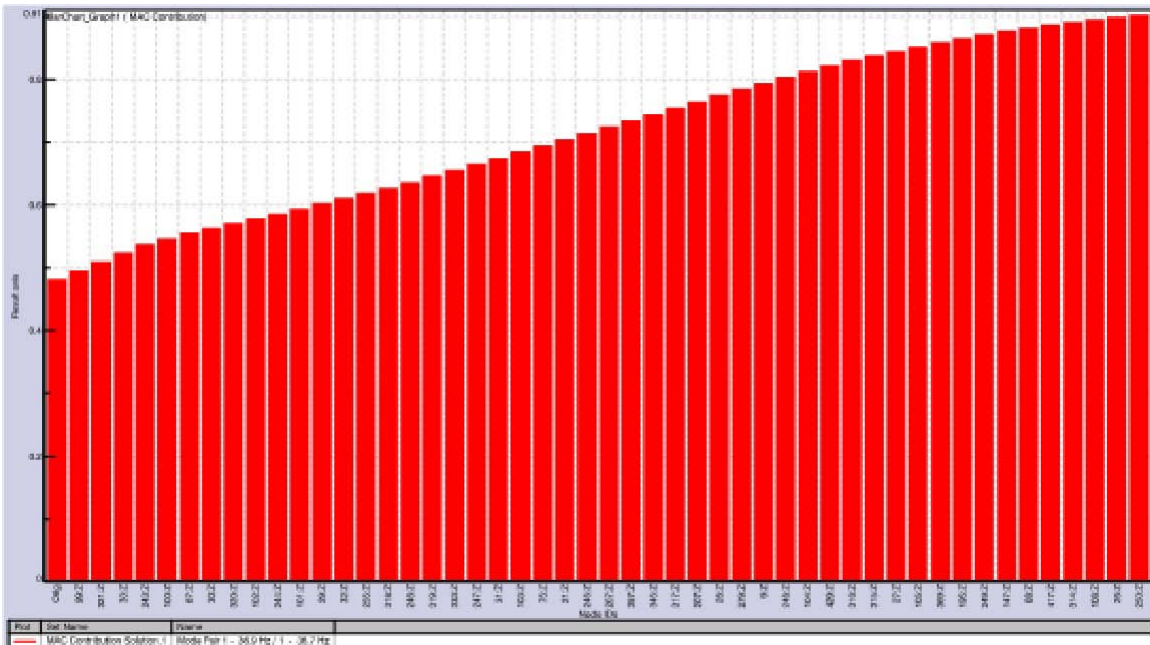

Figure 4.17: MAC Contribution for First Torsion (~37 Hz)

It can be seen here that the MAC value begins at 0.482 and climbs to 0.90 as DOF points are removed. Figure 4.18 illustrates the said removed points. It can be seen there that the points are of the outer perimeter, verifying the qualitative visual analysis.
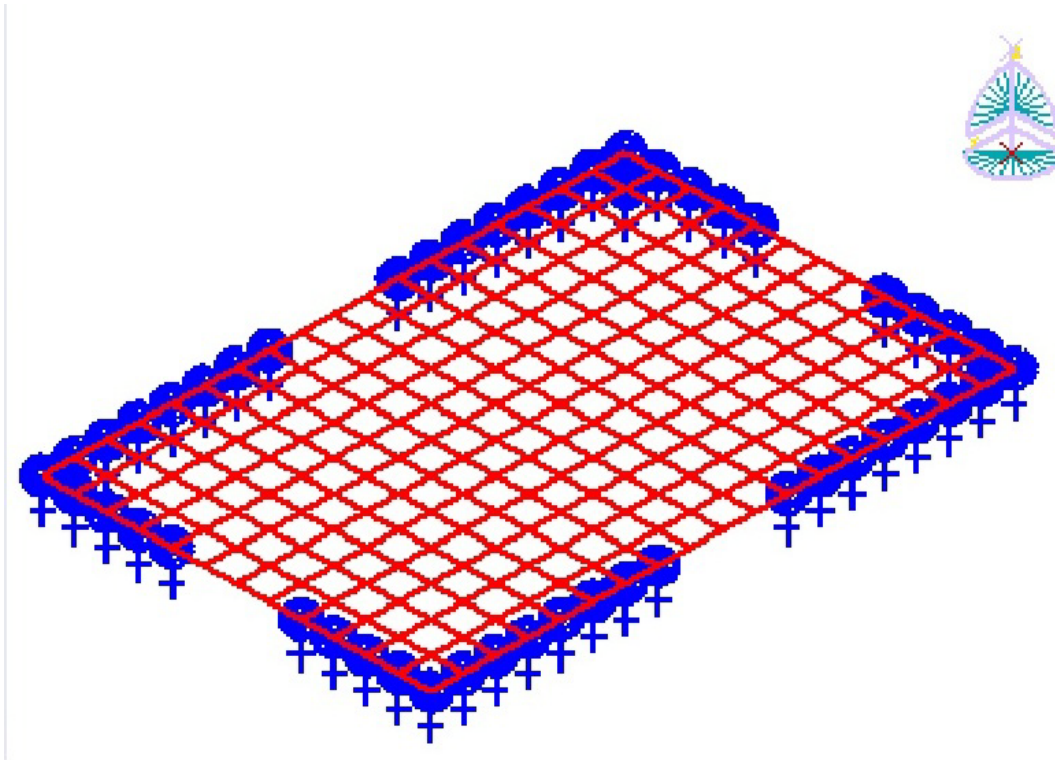

Figure 4.18: DOF Points Removed in MAC Contribution Analysis (~37 Hz)

The MAC contribution analysis was also done for the first bending mode. The similar results are shown in Figure 4.19 (MAC value climbing from 0.554 to 0.90) and the DOF points removed are shown in Figure 4.20 (outer perimter points only).
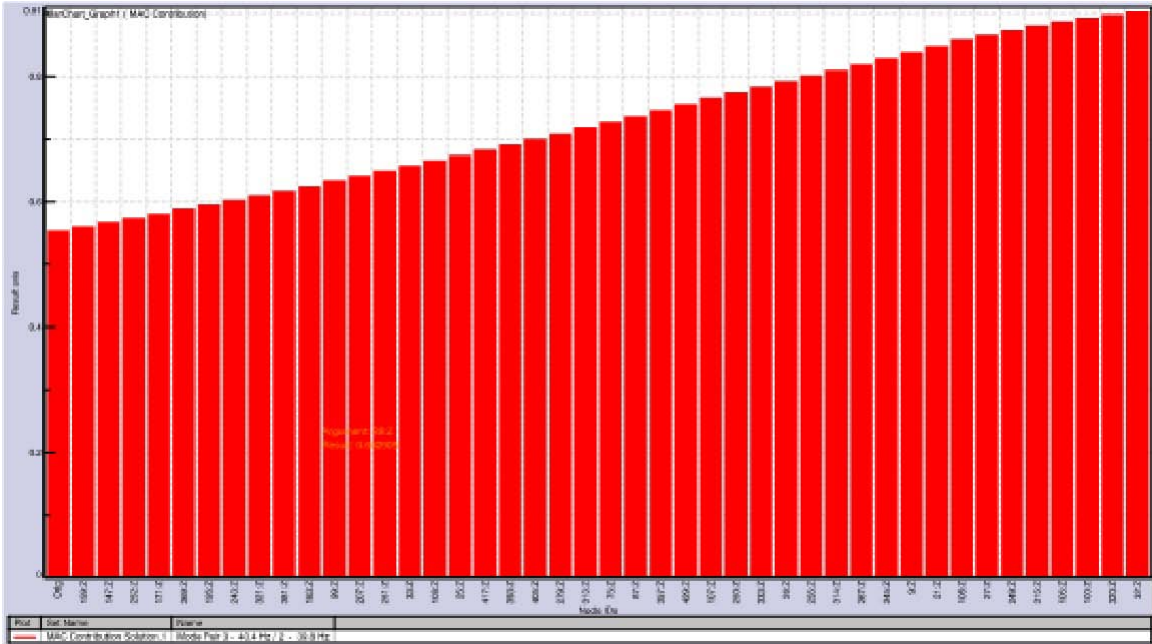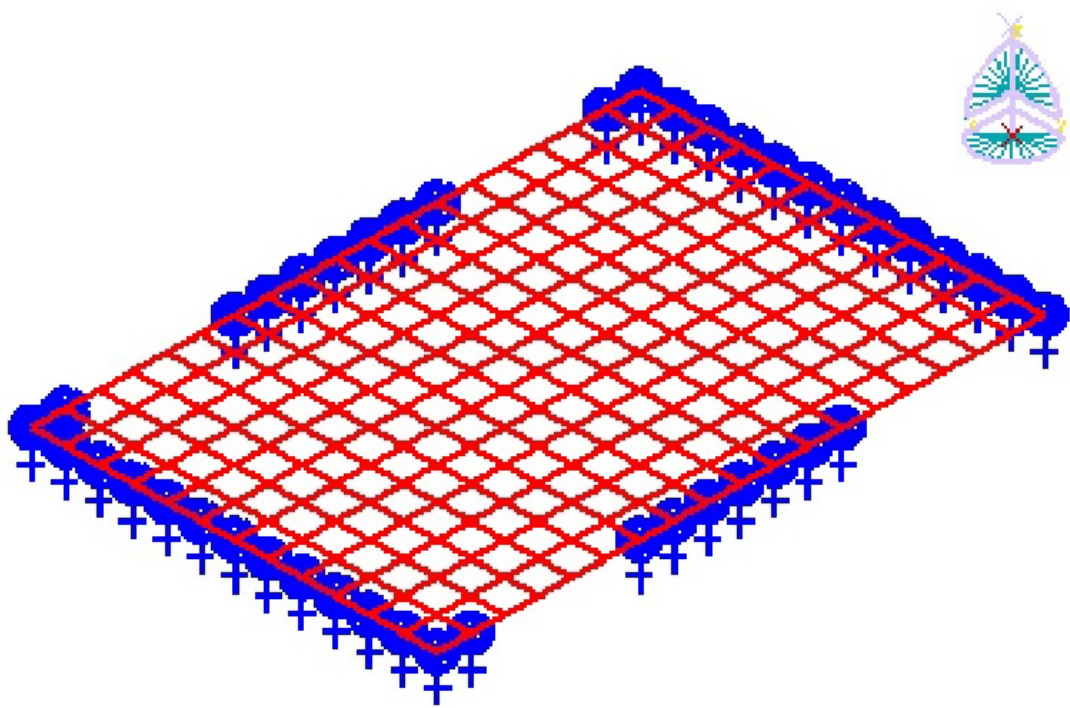
Figure 4.19: MAC Contribution for First Bending (~40 Hz)

Figure 4.20: DOF Points Removed in MAC Contribution Analysis (~40 Hz)

73

The mode shapes were also compared qualitatively. The following figures are a comparison of the FEA model, the Laser modal results and the NAH modal results. The FEA mode shapes are shown such that the blue to red map indicates out of plane motion in the positive direction. The light green mesh illustrates either no motion, or out of plane motion in the negative direction.

The first set of three examines the first torsion mode at ~37Hz:

Figure 4.21: FEA Mode Shape – first torsion
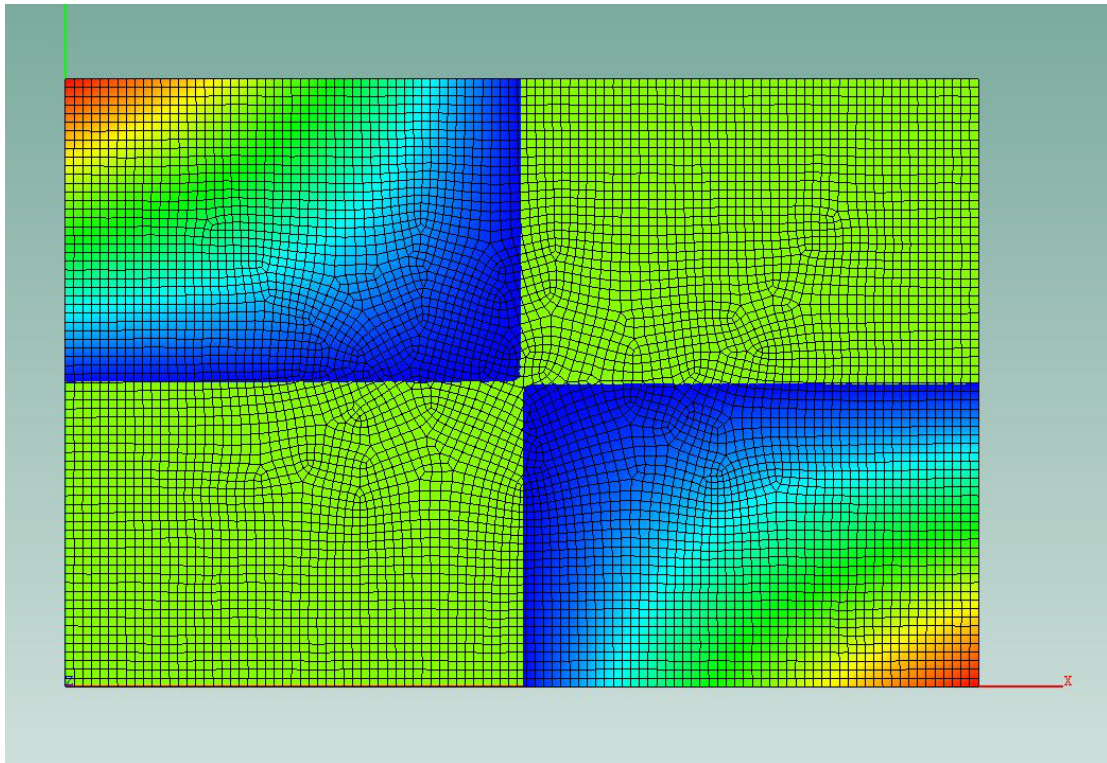
The FEA mode shapes show the motion as a color palette, with dark blue indicating the least out of plane motion and red indicating the most. The laser and NAH mode shapes

were taken from the viewer in Xmodal. The red dots indicate the static plate. The black, dots are the plate in motion.
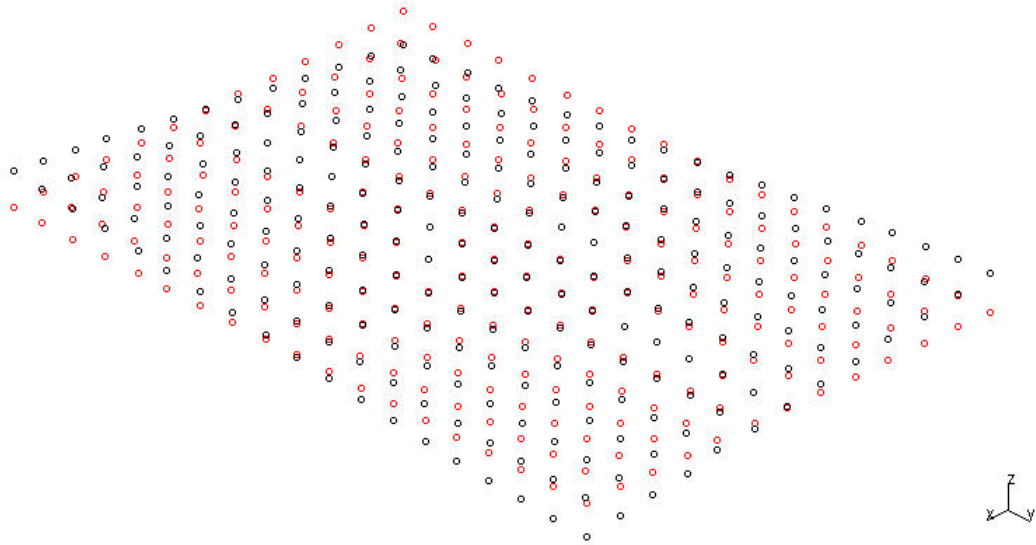
Figure 4.22: Laser mode shape – first torsion

Figure 4.23: NAH mode shape – first torsion

75

It can be seen in comparing Figures 4.22 and 4.23 that the outer perimeter of modal

points in the NAH mode shape has minimal to no motion. These points were removed to

compare the motion of the shape for the cross-MAC of Figure 4.13.

The next set of mode shapes is the first bending at approximately 40 Hz:
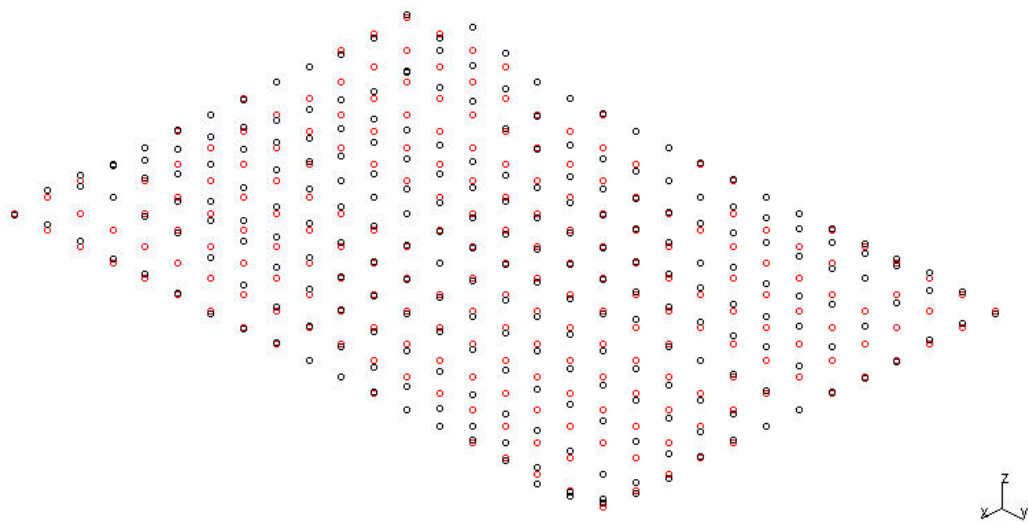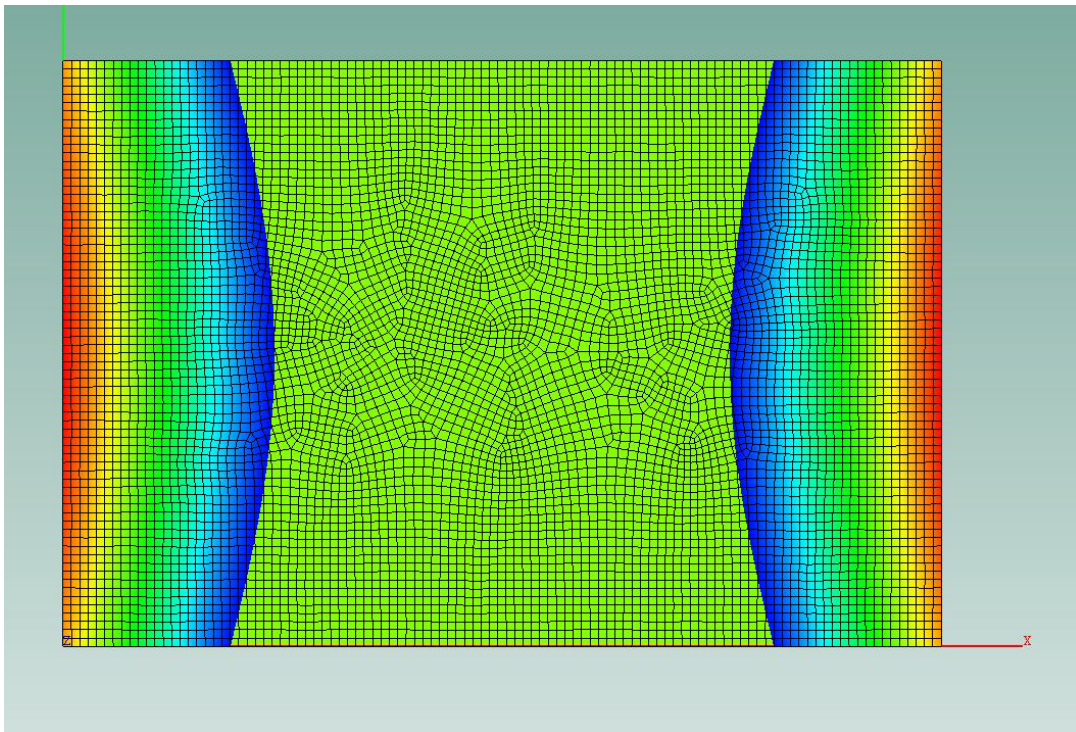

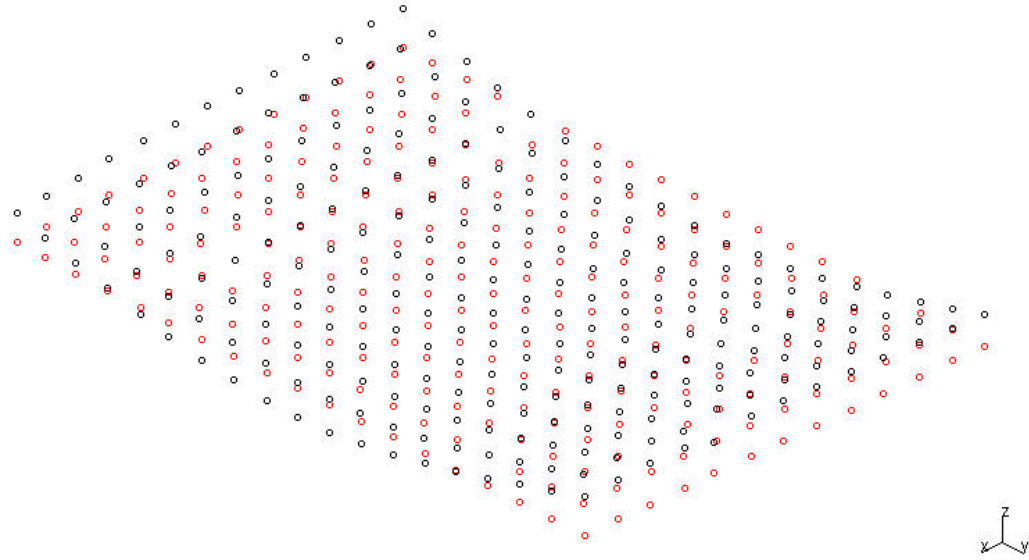Figure 4.24: FEA mode shape –first bending

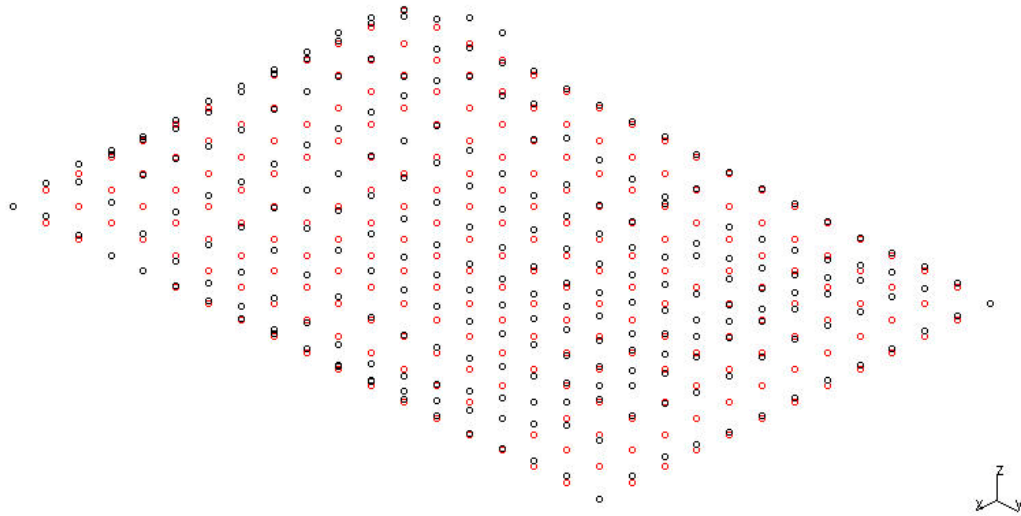Figure 4.25: Laser mode shape – first bending

Figure 4.26: NAH mode shape – first bending

Again the comparison between figures 4.19 and 4.20 shows that the outer perimeter of

the NAH mode shape has much less motion than the remainder of the modal points.

77

Chapter 5: Final Discussion

The research contained within this project focused on the comparison of modal analysis results when surface velocity of a vibrating aluminum plate was directly measured using Laser Vibrometry and when it was calculated using Nearfield Acoustical Holography sound pressure measurements. This chapter will discuss the conclusions of the project, as well as suggestions for related future work.

5.1 Conclusions

It has been shown that the Laser Vibrometer and NAH are well correlated methods for using surface velocity in modal analysis. The frequency results were within 2% between each experimental method, and as compared to the FE analysis. Damping values were not as close, with discrepancies up to 65% and Laser results producing higher values. The mode shapes, when compared without the outer perimeter of measurement locations agreed with MAC values on the order of 0.85. From this, it can be said that NAH is an acceptable method for determining frequency and mode shapes of a vibrating structure. More research is necessary to understand the difference in damping values. The test article, an aluminum plate hanging in free-free configuration, is as close to an ideal system as possible for this test. Because of this, the low damping values have high margin for error.

5.2 Recommendations

The first thing that should be investigated is the processing parameters of the NAH calculations to determine if there is, in fact, a scaling error that comes to be in the final scaled velocity over input autopower "FRF." As shown in Chapter 4, the NAH peak values of the "FRF" are higher than those of the Laser, and appear to be so by a constant factor.

An investigation into the NAH processing should also be completed regarding the edge effect. It is not understood why the Laser measured motion at the edge points, but NAH did not. It is possible that the energy of the plate was only enough to drive a microphone response in the NAH measurements, but not enough to register in the reconstruction of the hologram field at the surface of the plate. It is also not understood where the motion is "believable" between the edge point that is not moving and the first moving point of the NAH mode shapes.

NAH measurements should also be acquired using a different set of microphones that have better coherence below 80Hz. This will reduce the noise in the measurement, and will theoretically increase the MPC value of the first two mode shapes (first torsion and first bending). Furthermore, it would increase the MAC value between the Laser and NAH mode estimates at these lower frequency mode shapes.

An interesting study would be to determine the effect of spatial jitter in the NAH microphone measurements. Spatial noise affects the reconstruction of the hologram

surface, and while every effort is made to reduce the noise, an objective study to determine its affects would be beneficial.

References

(1) Polytec Scanning Vibrometer Theory Manual. [Internet]. Polytec International. Available from: http://www-mech.eng.cam.ac.uk/dynvib/lab_facilities/vibrometer_theory_manual.pdf

(2) What is traffic noise and how do we measure it? [Internet]. Near-field Techniques. WSDOT. Available from: http://www.wsdot.wa.gov/Projects/QuieterPavement/CommonQuestions.htm

(3) Marroquin, M, Noise Source Identification: A comparison of Seven Different Techniques. Journal of the Acoustical Society of America 2002;112(5):2372-2378.

(4) Maynard, JD, Williams, EG, Lee, Y, Nearfield Acoustic Holography: I. Theory of Generalized Holography and the Development of NAH. Journal of Acoustical Society of America. 1985;78(4):1395-1413.

(5) Aircraft Acoustic Holography. [Internet]. Michael James, Blue Ridge Research and Consulting. Available from: http://www.inceusa.org/node/140

(6) Martarelli, M, Revel, GM, and Tomasini, EP, Laser Doppler Vibrometry and Near-Field Acoustic Holography: Different Approaches for Surface Velocity Distribution Measurements. International Conference on Vibration Measurements by Laser Techniques. 2002.

(7) Hologram at MIT Museum. [Internet]. Meutia Chaerani. Available from: http://www.indrani.net

(8) Dumbacher, SM, Brown, DL, Blough, JR, Bono, RW, Practical Aspects of Making NAH Measurements, Society of Automotive Engineers. 1998.

(9) Bono, RW, Brown, DL, Dumbacher, SM, Comparison of Nearfield Acoustic Holography and Dual Microphone Intensity Measurements. The Modal Shop Technical Library.

(10) Williams, EG, Fourier Acoustics. London: Academic Press; 1999.

(11) Beranek, LL, Acoustics. New York, NY: McGraw-Hill Book Company, Inc. 1954.

(12) Allemang, RJ, Vibrations: Analytical and Experimental Modal Analysis. University of Cincinnati. UC-SDRL-CN-20-263-662. 1992.

(13) Heylen, W, Lammens, S, Sas, P, Modal Analysis Theory and Testing. Katholieke Universiteit Leuven, Belgium, 2003.

(14) Phillips, AW, Allemang, RJ, Application of Modal Scaling to the Pole Selection Phase of Parameter Estimation. Proceedings of the IMAC-XXVII; Paper #167. 2010.

(15) VA-One 2009 [Software]. (2009). Paris, France: ESI Group.

(16) Allemang, RJ, Phillips, AW, The Unified Matrix Polynomial Approach to Understanding Modal Parameter Estimation: An Update. University of Cincinnati, Structural Dynamics Research Lab.